

Variability and trend of the North West Australia rainfall: observations and coupled climate modeling

Ge Shi (1), Wenju Cai (2, 3, 4), Tim Cowan (2, 3, 4), and Joachim Ribbe (1), Leon
Rotstayn (2, 4), and Martin Dix (2, 4)

1. Department of Biological and Physical Sciences, University of Southern
Queensland, Toowoomba , Queensland 4350, Australia
2. CSIRO Marine and Atmospheric Research, 107 Station Street, Aspendale,
Vic, 3195, Australia
3. Water for a Healthy Country Flagship
4. Wealth from Oceans Flagship

Abstract

Since 1950, there has been an increase in rainfall over North West Australia (NWA), occurring mainly during the Southern Hemisphere (SH) summer season. A recent study using 20th century multi-member ensemble simulations in a global climate model forced with and without increasing anthropogenic aerosols suggests that the rainfall increase is attributable to increasing Northern Hemisphere aerosols. The present study investigates the dynamics of the observed trend toward increased rainfall and compares the observed trend with that generated in the model forced with increasing aerosols.

We find that the observed positive trend in rainfall is projected onto two modes of variability. The first mode is associated with an anomalously low mean sea level pressure (MSLP) off NWA instigated by the enhanced sea surface temperature (SST) gradients towards the coast. The associated cyclonic flows bring high moisture air to northern Australia, leading to an increase in rainfall. The second mode is associated with an anomalously high MSLP over much of the Australian continent; the anticyclonic circulation pattern with northwesterly flows west of 130°E and generally opposite flows in northeastern Australia, determine that when rainfall is anomalously high, west of 130°E, rainfall is anomalously low east of this longitude. The sum of the upward trends in these two modes compares well to the observed increasing trend pattern.

The modeled rainfall trend, however, is generated by a different process. The model suffers from an equatorial cold-tongue bias: the tongue of anomalies associated with El Niño-Southern Oscillation extends too far west into the eastern Indian Ocean. Consequently, there is an unrealistic relationship in the SH summer between Australian rainfall and eastern Indian Ocean SST: the rise in SST is associated with an increasing rainfall over NWA. In the presence of increasing aerosols, a significant SST increase occurs in the eastern tropical Indian Ocean. As a result, the modeled rainfall increase in the presence of aerosol forcing is accounted for by these unrealistic relationships. It is not clear whether, in a model without such defects, the observed trend can be generated by increasing aerosols. Thus, the impact of aerosols on Australian rainfall remains an open question.

1. Introduction

During the past 50 years, there has been an overall positive trend in rainfall over North West Australia (NWA), as can be seen from the annual-mean rainfall changes shown in Fig. 1. In an environment in which decadal-scale droughts have plagued most of the country, and the long-term rainfall over southern Australia is projected to decrease further, continued upward trends in rainfall may provide a source of future water resources in NWA. The observed annual increase is approximately 50% of the climatological value, compared with a 15% reduction over the southwest Western Australia (SWWA) through the same period (Cai and Cowan, 2006).

The strong regional contrast of the trend shown in Fig. 1 highlights the complexity of the climate drivers affecting Australian rainfall. The influence of the El Niño - Southern Oscillation (ENSO) has been known for many years, with El Niño (La Niña) events associated with anomalously low (high) rainfall over most of eastern Australia (e.g., McBride and Nicholls 1983; Ropelewski and Halpert, 1987; Ashok et al. 2007a). The connection between Indian Ocean sea surface temperature (SST) and Australian rainfall variations was pointed out by Nicholls (1989). More recent research has focused on a natural mode referred to as the Indian Ocean Dipole, or IOD (Saji et al. 1999), and its link to Australian wintertime rainfall variations in a broad band stretching from the northwest to the southeast of the continent (e.g., Ashok et al. 2003; Saji and Yamagata 2003; Cai et al. 2005a). To the south, the Southern Annular Mode (SAM, also known as the Antarctic Oscillation) is the dominant mode of the Southern Hemisphere (SH) extratropical circulation, operating beyond the weather scale (Kidson 1988; Karoly 1990; Thompson et al. 2000; Hartmann and Lo 1998). It has been linked to interannual and interdecadal rainfall variations over SWWA (e.g., Cai et al. 2005b; Hendon et al. 2006; Cai and Cowan 2006), while other studies have examined the linkage of SWWA rainfall with the Indian Ocean (Samuel et al. 2006; Verdon et al. 2005). However, little is known about the drivers of rainfall variability over NWA.

Considerable effort has been made to understand the dynamics of the drying trend over a

number of Australian regions (e.g., Smith 2004; Cai and Cowan 2006). For example, the observed rainfall decreases along the east Australia coast may reflect an increased frequency of El-Niño events in the late 20th century, which could be related to an increase in greenhouse gases; indeed, coupled atmosphere-ocean general circulation models (GCMs) forced by increasing atmospheric CO₂ have simulated an El-Niño-like warming pattern in the Pacific Ocean (e.g., Meehl and Washington 1996; Cai and Whetton, 2000). This suggests the possibility that the observed rainfall decrease might be attributable to an El Niño-like warming pattern, and that future average rainfall might be lower over eastern Australia. To the west, rainfall over SWWA may be in part linked to a shift of the SAM towards its “positive” state, with decreased sea level pressure (SLP) over Antarctica and increased SLP over the SH midlatitudes (Cai et al. 2003; Cai and Cowan 2006). It may also be linked to multi-decadal variability of the SAM (Cai et al. 2005b), and to land-cover change (Pitman et al. 2004). One such robust feature of the SH response of coupled GCMs to an increase of greenhouse gases is a strengthening (weakening) of the circumpolar (midlatitude) westerlies. (Fyfe et al., 1999; Kushner et al. 2002; Cubasch et al. 2001; Cai et al., 2003); to

By contrast, there is relatively little understanding of the dynamics of NWA rainfall variability and trends. Two recent studies have shed some light. Wardle and Smith (2004) hypothesized that during the latter half of the 20th century, the observed increase in temperature gradient between Australia and neighbouring oceans drove a stronger monsoonal circulation. They found that by artificially altering this contrast through a change to the land albedo in a model, they could simulate an increase in rainfall over the entire continent, with stronger totals over the north. Their experiment also resulted in a temperature response similar to the observed. They concluded that the temperature changes were possibly leading to a strengthening of the monsoon and that this was the cause of the increased rainfall. However, the prescribed changes were much larger than could be justified based on current knowledge, so the authors left the cause of the land-ocean temperature contrast as an open question.

An alternative explanation for the increased northwest rainfall was provided by Rotstayn

et al. (2007) who, by using simulations from a low resolution coupled GCM, demonstrated that including (excluding) anthropogenic aerosol changes in 20th century gives increasing (decreasing) rainfall and cloudiness over Australia during 1951–1996. Rotstayn et al. (2007) showed that the pattern of increasing rainfall when aerosols are included is strongest over NWA, in agreement with the observed trends. The strong impact of aerosols is predominantly due to the massive Asian aerosol haze, as confirmed by a sensitivity test in which only Asian anthropogenic aerosols are included. The Asian haze alters the north-south temperature and pressure gradients over the tropical Indian Ocean in the model, thereby increasing the tendency of monsoonal winds to flow towards Australia.

The argument of an impact from aerosols seems to be supported by the fact that transient climate model simulations forced only by increased greenhouse gases, without the inclusion of aerosol forcing, have generally not reproduced the observed rainfall increase over northwestern and central Australia. Whetton et al. (1996) compared rainfall changes in five enhanced greenhouse climate simulations that used coupled GCMs, and five that used atmospheric GCMs with mixed-layer ocean models. The coupled experiments mostly gave a decrease in summertime rainfall over northwestern and central Australia, whereas the mixed-layer experiments mostly gave an increase (in better agreement with the observed 20th century trends). They attribute the difference to the coupled model feature that a stronger overall warming occurs in the Northern Hemisphere (NH) than in the SH, which is expected to lead to a similar hemispheric imbalance in rainfall (Murphy and Mitchell, 1995). The hemispheric asymmetry in warming is due to the greater proportion of ocean in the SH, and much greater thermal inertia of the SH oceans causing a delayed warming relative to the NH (Stouffer et al. 1989, Cai et al. 2003).

In the present study, we use available observations and reanalysis data to examine the dynamics of observed rainfall variability over NWA and circulation patterns associated with the observed increasing rainfall trend. We then benchmark the performance of the climate model used in the Rotstayn et al. (2007) study. We focus on whether the model reproduces the observed variability and circulation trend associated with the increased

rainfall (section 3). We show that the modeled rainfall change over NWA in the Rotstayn et al. (2007) study might be a by-product of a well-known model deficiency associated with an equatorial Pacific cold tongue, common in most climate models. The cold tongue extends into the eastern Indian Ocean (EIO), generating an unrealistic relationship between the EIO SST and Australian rainfall (section 4).

2. Data, methodology, and model experiments

2.1a Data

It is increasingly recognized that anthropogenic climate change can project onto existing natural variability modes of the climate system (Clarke et al. 2001). Thus it is important to understand the dynamics of rainfall variability over NWA. To this end we employ available observational data and reanalysis. The observed rainfall data we use are from the Australian Bureau of Meteorology Research Centre (BMRC) and Global Sea Ice and Sea Surface Temperature (GISST) datasets. Although these two datasets cover a period from late 19th century, we focus on the 50 year period from 1951-2000. To understand the circulation associated with rainfall patterns, SLP and surface winds data, and other fields from the National Centers for Environmental Prediction (NCEP) reanalysis are used (Kalnay et al. 1996). Seasonal anomalies are constructed for each season into December-January-February (DJF), March-April-May (MAM), June-July-August (JJA), and September-October-November (SON), referenced to the respective seasonal average over 1951-2000.

2.1b Methodology

Empirical orthogonal function (EOF) spatial patterns and time amplitude functions are calculated to assess the variability pattern of both SST and rainfall. We use a covariance EOF, and the variance of the time amplitude function of an EOF sums to unity, leaving the variance of an EOF to be recorded in the spatial pattern. The inter-relationship

between various circulation patterns is obtained by regressing/correlating grid-point anomalies of a field onto an index of a given pattern, for example, the time amplitude function of an EOF, or Nino3.4 (170°W-120°W, 5°S-5°N, an index of ENSO).

We also use a linear projection method to investigate the evolution of a given circulation pattern $G(x,y)$ and the extent to which climate change signals project onto the given pattern. For a circulation field $A(x,y,t)$, this is carried out in the following way: for each given instant t_n , we regress $A(x,y, t_n)$ onto $G(x,y)$ to yield a pattern regression coefficient. When this is done for all t , a time series $f(t)$ of the pattern regression coefficient is generated. The time series $f(t)$ is employed to estimate the trend $\nabla f(t)$ of the pattern, and the trend associated with the pattern is given by $\nabla f(t) \times G(x,y)$. We first explore modes of variability using linearly detrended data. We then project raw data onto these modes of variability to assess whether the observed rainfall increase over NWA can be understood in terms of a projection onto the existing variability modes.

2.1c Model outputs

One of the aims of the present study is to examine if the rainfall trend produced in the CSIRO Mk3a model forced with all climate change forcings, including increasing aerosols, is generated by the same processes as in the observations. As detailed in Rotstayn et al. (2007), these set of simulations are run with a comprehensive aerosol scheme and cover the period 1871 to 2000. The aerosol species treated interactively are sulfate, particulate organic matter (POM), black carbon (BC), mineral dust and sea salt. As well as the direct effects of these aerosols on shortwave radiation, the indirect effects of sulfate, POM and sea salt on liquid-water clouds are included in the model. Historical emission inventories are used for sulfur, POM and BC derived from the burning of fossil fuels and biomass. Other forcings included are those due to changes in long-lived greenhouse gases, ozone, volcanic aerosol and solar variations (but changes in land cover are omitted). The ensemble consists of eight runs with all of these forcings (ALL ensemble). A further eight runs with all forcings except those related to anthropogenic aerosols (AXA ensemble), differing only from the ALL ensemble in that the

anthropogenic emissions of sulfur, POM and BC were fixed at their 1870 levels, produce a decreasing rainfall trend in NWA.

We take outputs from a multicentury (300 years) control experiment (without climate change forcing) to examine if the model reproduces the rainfall teleconnection with large scale circulation fields. We then project outputs from the ALL ensemble onto modes of variability in the control experiment, in the same way as for the observed. The result is that the process by which the modeled rainfall increase is generated is rather different from that in the observed.

3. Observed trend and variability of NWA rainfall

3.1 Seasonal stratification of trends and variability

NWA is a warm-month rainfall region, and is strongly influenced by the Australian summer monsoon. As such, most of the annual total rain is recorded in summer; summer rainfall is about ten times greater than in the winter season (Fig. 2, left column). In association, although the trend over NWA shows up in the annual mean map, it is primarily a summertime (DJF) phenomenon (Fig. 2e, right column). The percentage (figure not shown) of increase is also substantial; over most of NWA the increase is greater than 20% over the past 50 years. By contrast, a reduction occurs over most of eastern Australia in DJF. In other seasons, the trend over NWA is small in absolute terms. The decreasing rainfall trend over eastern Australia (25°S southward) shown in Fig. 1, occurs mainly in the JJA season.

In order to understand the dynamics of the rainfall trend it is necessary to examine the dynamics of rainfall variability as the response to a climate change forcing that might project onto the existing modes of variability. To this end we use linearly detrended data. Rainfall variability over Australia is region-specific as variability can be predominately driven by one of the global-scale modes of variability, while simultaneously affected by other modes. Further, the relative importance of these modes varies with season, as will

be clear in the ensuing analysis, necessary for benchmarking the performance of the model used by Rotstayn et al. (2007).

Fig. 3 shows maps of correlation between the observed NWA rainfall (averaged over 110°E-135°E, 10°S-25°S – land points only) and grid-point global SST for each season. In DJF (Fig. 3a), although the correlation pattern in the Pacific displays a La Niña-like pattern, most of the correlation coefficients have an absolute value of less than 0.27, a threshold required for a 95% level of statistical significance. Correlation between the NWA detrended rainfall time series and detrended Nino3.4 index records a coefficient of 0.29, marginally greater than the value for 95% statistical significance. The weak correlation is consistent with the canonical Australian rainfall-ENSO relationship (e.g., Ropelewski and Halpert 1987), which depicts an influence mostly over eastern Australia. In the Indian Ocean, the correlation is generally greater than in the Pacific. As will be shown, the overall pattern is similar to that associated with a La Niña phase. In particular, an east-west temperature gradient along 20°S is rather prominent with cooling taking place off the WA coast, and relative warming along the coast.

In MAM there is little significant correlation between NWA rainfall and SST (Fig. 3b). The overall pattern is one that evolves from Fig. 3a, with a decaying La Niña in the Pacific, and westward propagating anomalies in the southern tropical Indian Ocean. In JJA (Fig. 3c), the correlation is much stronger and with a well-defined correlation pattern, resembling the map Nicholls (1989) obtained by correlating southeastern Australian rainfall with SST anomalies in the Indian Ocean. Recent studies have shown that this pattern can evolve into an Indian Ocean Dipole (IOD) – a coupled ocean-atmospheric phenomenon (Saji et al., 1999), which usually starts in JJA and peaks in SON. The IOD linkage to Australian wintertime rainfall variations has been explored recently, and is found to consist of a broad band stretching from the eastern Indian Ocean, to the northwest and southeast of the continent (e.g., Ashok et al. 2003, Cai et al. 2005a). This is reproduced here (Figs. 3c and 3d). Since 1950, some IOD events occur coherently with an ENSO event, due to their seasonal phase-locking properties (Yamagata et al., 2004),

giving rise to the strong ENSO-like pattern in the Pacific (Fig. 3d), with the majority of correlations statistically significant at the 95% level.

The above analysis indicates a strong linkage of NWA JJA and SON rainfall with the IOD and ENSO, but such a linkage is weak in DJF. In particular, warm Indian Ocean SSTs in DJF are not associated with an increase in NWA rainfall (Fig. 3a). To further illustrate this, we take a time series of seasonal-mean Nino3.4 and EIO SST anomalies (averaged over 90°E-110°E, 5°S-15°S), and correlate them with grid-point rainfall anomalies of the same season. The results are shown in the left column of Fig. 4 (red colour indicating drier-than-normal conditions) for Nino3.4 and the right column for EIO SST. We have also calculated correlation with Nino3 (5°S-5°N, 90°W-150°W), we find that the correlation maps are similar, consistent with the finding of a recent study (Ashok et al., 2007b).

In DJF (Fig. 4, left column) ENSO has a weak effect on NWA rainfall, with warmer SST in the equatorial eastern Pacific tending to reduce NWA rainfall. A sizable correlation exists in a strip extending from central northern Australia to the southeastern regions. In eastern Australia, a significant correlation is seen; this is the well-known ENSO-eastern Australia rainfall teleconnection (McBride and Nicholls 1983; Ropelewski and Halpert 1987). In MAM, large correlations are seen in the central southern region. In JJA and SON, a positive Nino3.4 index is associated with decreasing rainfall over central eastern Australia.

In DJF, EIO SST anomalies tend to influence rainfall over inland Australia (Fig. 4a, right column) with an increase in EIO SST associated with a decrease in rainfall; the pattern is similar to that associated with Nino3.4, although the influence (Fig. 4a, left column) is not completely identical. The pattern which stretches from the central northern inland region to the southeastern inland regions reappears with stronger correlations. However, the influence over NWA is rather weak. If anything, an increase in the EIO SST trend is associated with a decrease in NWA rainfall.

In the MAM season, the impact of the EIO SST on NWA rainfall tends to be opposite to that in DJF, but is rather weaker, as indicated by lower correlation coefficients. In the JJA and SON seasons (right column, Figs. 4g and 4h), increasing EIO SSTs are strongly associated with rainfall increases in southern Australia (JJA) and parts of NWA (SON). Note that in SON the rainfall correlation pattern with EIO SSTs strongly resembles that associated with Nino3.4 but with opposing polarities in the correlation coefficients (Figs. 4d and 4h, left and right columns).

Thus, the significant correlation between NWA rainfall with known modes of global SST variability only occurs in the JJA and SON seasons, when there is little trend in rainfall. In DJF the correlation with either ENSO or IOD is rather weak.

3.2 Variability of DJF rainfall and Indo-Pacific SSTs

In this section, we will focus on the DJF rainfall variability. To examine the possibility of a mode of DJF SST variability that dominates the NWA DJF rainfall, we conduct EOF analysis on detrended DJF SST anomalies in the tropical Indian Ocean domain over the 1951-2000 period. We perform the analysis over this domain, as opposed to the whole Indo-Pacific region, because we are interested in the teleconnections influencing NWA rainfall through the tropical Indian Ocean. The first mode accounts for 37.2% of the total variance and mainly reflects variations associated with ENSO (Cai et al. 2005a), with warm anomalies occupying almost the entire Indian Ocean basin. The correlation between the associated time series and Nino3.4 for the SST EOF1 in the tropical Indo-Pacific domain is as high as 0.89. The EOF1 is the well-known basin-scale pattern resulting from atmospheric teleconnection with the Pacific. For a comparison with the model ENSO in section 4, the anomaly patterns of wind and SST associated with El Niño are plotted in Fig. 5. An El Niño event generates easterly anomalies throughout much of the tropical (10°S -10°N) Indian Ocean (Fig. 5), which superimpose on the climatological westerlies, giving rise to a warming and decreased evaporation. The opposite occurs during La Niña. The correlation between the EOF1 time series and rainfall is fairly

similar to that associated with Nino3.4 (Fig. 4a, left column); the correlation is rather weak over NWA.

The pattern of EOF2, which accounts for 14.9% of the total variance, depicts positive anomalies extending northwest from the NWA coast into the Indian Ocean. The pattern of correlation coefficients between the time series and Australian rainfall show a general opposite polarity between east and west of 130°E, with the correlations bordering on 95% statistical significance. We shall discuss the linkage of EOF2 with NWA rainfall later, when we analyse NWA rainfall EOFs.

The above results suggest that there is no well-defined SST EOF mode that dominates the NWA DJF rainfall variability, and there is a weak ENSO influence on NWA rainfall. In any case, the trend of ENSO over 1951-2000 is certainly unable to explain the observed DJF rainfall trend, because there is an upward trend in Nino3.4 over the 50-year period. According to the ENSO-NWA rainfall relationship shown in Fig. 4a (left column), i.e., an increase in rainfall is associated with a La Niña pattern; the upward trend in the Nino3.4 would mean a rainfall reduction rather than an increase. Indeed, removing the influence of ENSO results in an even stronger increasing rainfall trend. For these reasons we will remove ENSO in our subsequent analysis. To this end, we linearly regress DJF rainfall anomalies onto Nino3.4 and remove the associated anomalies identified.

Since we are unable to identify entities of SST patterns that are responsible for DJF rainfall variability, and since ENSO is not responsible for the positive trend in NWA rainfall, we remove ENSO signals at all grid points. We conduct EOF analysis on the non-ENSO NWA rainfall anomalies in the domain of 110°E-135°E, 10°S-25°S. The EOF1 accounts for 47.2% of the total variance, and EOF2 accounts for 12.2% of the total variance (without ENSO). We focus on this limited region rather than Australia-wide because the trend is concentrated in this limited area.

To find out the associated pan-Australia pattern, grid-point rainfall anomalies are regressed onto the associated time series, with the patterns shown in Fig. 6. The EOF1

spatial pattern reflects the northern-concentration of variance, with small anomalies south of 28°S. The EOF2 pattern (Fig. 6b) shows coherence between the regions east and west of 130°E, but of opposing polarities; to the east, anomalies are strongest north of 25°S, and to the west anomalies are largest in the area between 112°E-125°E, 18°S-26°S. As will be shown, the increasing rainfall trend over NWA is a result of the upward trends of these two modes, east of 130°E, and the weights that EOF1 and EOF2 offset, giving rise to the spatial feature shown in Fig. 2e (When similar analysis is conducted with the presence of ENSO signals in rainfall, similar patterns emerge, supporting the small impact of ENSO on rainfall in the region. The correlation between the EOF1 time series and Nino3.4 is 0.28, and between the EOF2 time series and Nino3.4 is 0.02, virtually independent from ENSO.)

To obtain the SST pattern associated with the rainfall EOF without ENSO, we regress grid-point SST anomalies onto the two EOF time series with the results shown in Fig. 7. The regression pattern for EOF1 (Fig. 7a) is somewhat similar to that associated with Nino3.4 (Fig. 5), taking into account of opposite signs. The pattern is also similar to that identified by England et al. (2006, their Fig. 5) associated with extreme rainfall events over SWWA, although in the present context we are dealing with all rainfall events. The associated anomalies are not spatially uniform, and encompass enhanced east-west gradients toward the NWA coast. It is the change of the SST gradient, not the SST *per se*, that generates NWA rainfall variability. Fig. 7a shows that an increased zonal SST gradient toward the NWA coast is conducive to rainfall increase over northern Australia. The SST pattern associated with EOF2 (Fig. 7b) indicates that warming anomalies off west and northwestern Australia promote rainfall over NWA west of 130°E, but are associated with a rainfall reduction east of this longitude.

The fact that the Indian Ocean SST pattern associated with the rainfall EOF1 without ENSO resembles the pattern associated with ENSO, yet the associated rainfall is rather different (Fig. 3a (left column) vs. Fig.6a) raises two important issues. First, patterns of SST variability independent of, but similar to that of ENSO can have a significant influence on NWA rainfall. Second, the influence on rainfall by this pattern is dependent

on the equatorial Indo-Pacific SST anomaly structure. In the presence of a La Niña (Fig. 3a), the impact is vastly different from that without a La Niña (Fig. 6a).

To further understand the dynamical processes of the two rainfall EOFs, we regress NCEP MSLP, surface winds, and cloud cover anomalies onto the two rainfall EOF time series and plot the results in Figs. 8 and 9. Figure 8a indicates that the rainfall EOF1 is associated with a decreased MSLP bordering the northwest coast, with a cyclonic flow pattern consisting of northwesterlies blowing from the EIO (10°S) towards the NWA coast, with strong northerlies toward northern Australia. These winds pick up the high moisture content from the tropical ocean, leading to an increase in northern Australian rainfall. In association, a pattern of increased cloud cover is seen over NWA (Fig. 9a) which occupies the entire northern Australia region, consistent with the rainfall EOF1 pattern. Note that in this season the climatological mean winds are westerlies, therefore the northwesterlies blowing from the EIO at 10°S act to enhance the westerlies and evaporation (figure not shown), generating a cooling (Fig. 7a) in the tropical EIO. In this way, increasing rainfall over northern Australia is associated with anomalously low EIO SST. Other large scale features seen in Fig. 8a include strong southeasterly flows extending from the WA coast into the central southern subtropical Indian Ocean, and the flows are supported by an anomalously high MSLP to the west and near-coast low MSLP. As discussed previously, it is the gradient of SST that is important in moving tropical convection, rather than the absolute value of SST (indeed there are small anomalies along the NWA coast, Fig. 7a). The strong southeasterly flows in the subtropical Indian Ocean are conducive for the cooling offshore seen in Fig. 7a; indirectly contributing to the enhancement of zonal SST gradients towards the NWA coast.

The anomalous circulation associated with the rainfall EOF2, shown in Fig. 8b, is rather different. MSLP tends to be higher over the Australian continent. The associated flow pattern shows that, east of 130°E, northwesterly flows towards the tropical EIO are generated, some veer eastward, and as part of an anticyclonic pattern, turn south along the WA coast, and pick up moisture over the ocean along the way. These northerlies with high moisture impinge on the NWA coast and contribute to the high rainfall west of the

130°E, whereas eastwards the flows are generally southwesterly over northeastern Australia. In this way, rainfall is high west of 130°E, and low to the east. The cloud cover pattern (Fig. 9b) shows an increased cover extending from subtropical EIO southeastwards to 130°E, however looking east decreased cloud cover is seen over northern Australia.

It will be shown in Section 4 that these two rainfall modes and the associated DJF circulation pattern are generally well reproduced by the CSIRO model. However, the model also generates unrealistic circulation modes in this season.

3.3 The dynamics of the observed DJF rainfall trend

In this section we focus on the NWA rainfall trend in DJF. We have shown that the trend in ENSO over the past 50 years is unable to explain the DJF rainfall trend, and that there is no SST mode of variability in this season identifiable by EOF analysis that dominates NWA rainfall variability. Can we understand the rainfall increase in terms of the two rainfall EOFs identified in section 3.2? To this end, we project DJF rainfall anomalies onto the EOF1 and EOF2 patterns following the procedure described in Section 2. Firstly, for each year, the raw DJF observed rainfall anomaly pattern is linearly regressed onto the DJF rain EOF1 pattern in the domain of 110°E-135°E, 10°S-25°S. This is conducted for 50 years from 1951-2000, and a time series of regression coefficients is generated, which shows an upward trend. Secondly, the total trend in the time series, $\nabla f(t)$, is calculated through linear trend analysis. Finally, the trend associated with EOF1 is obtained by multiplying the total trend in the time series $\nabla f(t)$ with the EOF1 pattern (Fig. 6a). The result is plotted in Fig. 10a. A similar analysis is conducted for EOF2; the time series again displays an upward trend. The trend due to EOF2 is shown in Fig. 10b. The sum of EOF1 and EOF2 (Fig. 10c) produces an amplitude and shape of the trend that compares quite well with the total trend over NWA (Fig. 2e). The amplitude of the trend is larger than that shown in Fig. 2e in some places. Thus the DJF rainfall increase over NWA can be understood in terms of the upward trend of the two EOFs combined. This

combination is important because it generates the shape with a northeast-southwest orientation.

In the above analysis, we have excluded the trend in ENSO. We now include this by regressing detrended rainfall onto the detrended Nino3.4 and then multiplying the regression pattern with the trend in the raw Nino3.4. When this is included, it does not change the overall trend pattern (Fig. 10d), consistent with the fact that the impact of ENSO is small. However, as the ENSO trend over the past 50-years serves to decrease NWA rainfall, the inclusion of the impact of an ENSO-like pattern further improves the agreement with the total trend (Fig. 2e). In particular, it is the ENSO-like pattern that is principally responsible for the decreasing rainfall trend over the coastal eastern Australia.

A similar approach is used to calculate the trend in SST associated with the two rainfall EOFs. We regress undetrended SST anomalies onto the SST patterns shown in Fig. 7 for DJF of each year in the domain of 40°E-120°E, 40°S-40°N. A time series of the regression coefficient is obtained and the total trend is calculated. The trend maps for EOF1 and EOF2 are similar to those shown in Fig. 7. As in the rainfall trend, the associated SST trend is dominated by that associated with EOF1. The combined SST trend pattern is shown in Fig. 11a, and illustrates a strong zonal SST gradient toward the WA coast.

This result suggests that over the past 50 years, ocean warming has projected onto the SST patterns associated with NWA rainfall variability encapsulated in the two rainfall EOFs. This is further illustrated by comparing the total trend obtained through linear regression of the raw SST anomalies (Fig. 11b). A pattern of greater warming along the WA coast, and hence a greater zonal SST gradient towards WA coast is evident. This gradient in Fig. 11a reaches about 0.4°C over 40° longitude (80°E to 120°E) and is comparable to that in the raw data, taking into account that there is an overall warming in the latter plot. Significant warming has occurred north of about 10°S, the dynamics of which is not clear, but in this season, this particular warming does not contribute to a rainfall increase over NWA (Fig. 3a).

Similarly, we have projected MSLP anomalies on the MSLP patterns shown in Fig. 8. The total trend associated with the two rainfall EOFs is shown in Fig. 11c, to be compared with the total trend (Fig. 11d). Given that it is the pressure gradient that drives the wind, to facilitate a comparison, a uniform value 1.4 mb is subtracted everywhere. We see that the patterns are very similar supporting that a climate change signal has projected onto existing modes of rainfall variability to generate the rainfall increasing trend.

Before we leave this section, a brief summary is in order. We have shown that in DJF there is no known SST variability mode that dominates the observed positive trend in NWA rainfall. Further, the El Niño-like trend pattern over the past 50-years acts to decrease the NWA rainfall, therefore it is unable to explain the observed increase. Instead we find that the rainfall increase is attributable to an intensification in SST gradients towards the coast, west of 130°E. In what ensues, we examine the CSIRO climate model experiments described by Rotstayn et al. (2007) to see if the same process is responsible for an increase in NWA rainfall.

4. Model rainfall variability and trend

Before we proceed to discuss the model results, we stress that the model is at a low-resolution and suffers from a common problem in the equatorial Pacific, which is too cold and extends too far into the western Pacific. In addition, the model ENSO is too weak; the standard deviation is about one third of the observed. The period is too long; the spectrum has the highest power on the 8-12 years, instead of the observed 3-7 years. We first described the trend averaged over the eight-experiments with all forcing including increasing aerosols (ALL). We then use a 300-year long control experiment, i.e. without climate change forcing, to examine the variability of NWA rainfall in ways similar to those conducted for the observed. Finally we analyse outputs from the ALL ensemble to examine if the rainfall trend is generated in the manner similar to that observed.

4.1a Seasonal trends

As in the observed, the model NWA rainfall mainly occurs in summer months with most of the annual total rain recorded in DJF; in fact, the DJF total rainfall is more than ten times as large as in the JJA total (Fig. 12, left column), and the climatological total compares well with the observed. In association, most of the rainfall increase takes place primarily in DJF (Fig. 12, right column). However the increase is much broader, including the eastern Australian region, inconsistent with the observed rainfall.

We will try to understand the dynamics of rainfall variability using a multi-century control experiment. In this experiment there is virtually no trend, so detrending analysis is not required. The anomalies are constructed with reference to the mean over the 300 years.

4.1b Seasonal correlation between NWA rainfall and global SST

Figure 13 shows maps of correlations between model NWA rainfall and grid-point SST anomalies as in the observed (compared with Fig. 3 for the observed). For the DJF season (Fig. 13a), the correlation pattern in the Pacific displays a model La Niña-like pattern. Unlike the observed, most of the correlation coefficients have an absolute value greater than 0.12, a threshold required for a 95% level of statistical significance. In particular, the correlation with the eastern Pacific is rather high, generally greater than 0.4. The high correlation suggests that the model NWA rainfall is overly influenced by the model ENSO, a feature that is rather unrealistic. As will be clear this is a consequence of the cold tongue problem, which extends into the equatorial EIO, where the correlation pattern shows a negative phase of an IOD-like pattern. The warm anomalies in the EIO then contribute to an anomalously high rainfall over NWA. Such an IOD-like pattern in DJF is absent in the observations (Fig. 3a).

The correlation pattern for MAM (Fig. 13b) shows a similar pattern to that in DJF. Again the correlations with SST in the equatorial Pacific and the eastern Indian Ocean are unrealistically too strong. In the JJA and SON seasons (Figs. 13c and 13d), the correlation patterns in the Indian Ocean resemble the observed and reflect basically the IOD-like variation pattern.

Overall, there are several major differences between the model and the observed. Firstly, in the observed, the IOD pattern only appears in JJA and SON, whereas in the model, an IOD pattern appears to operate in all seasons. Secondly, in DJF the observed NWA rainfall shows a weak correlation with ENSO, whereas in the model, correlation with ENSO is far greater. Finally, in SON, the correlation of NWA rainfall with equatorial Pacific SST is weaker than that in the observed.

The model IOD-like variability pattern in DJF and MAM (Figs. 13a and Fig. 13b) is rather unrealistic. In reality, development of the IOD (with cold anomalies off the Sumatra–Java coast) occurs only in JJA and SON (Rao et al. 2002). Because the climatological mean winds in the eastern Indian Ocean are easterly south of the equator during JJA, the thermocline is located at a shallower depth. The El Niño-induced easterlies act to increase the wind speed and the latent and sensible heat fluxes. Increased upwelling and stronger latent and sensible heat fluxes overcome the increased shortwave radiation associated with reduced rainfall, leading to the development of a cold pool. The demise of the IOD typically occurs in December after the Australian summer monsoon commences, when the mean winds become westerly in the equatorial EIO, and the thermocline is deepened so that there is little thermocline-SST coupling. The induced easterly anomalies then act to reduce the wind speed. Reduced latent heat flux and increased surface shortwave radiation act together to warm the Indian Ocean, yielding a basin-scale warm anomaly (e.g., Klein et al. 1999).

It is beyond the scope of the present study to fully explore the dynamics of the IOD in this model. However, it is apparent that the IOD-like variability pattern is a consequence of the model cold tongue that extends too far west, and in this version of the model, into

the Sumatra-Java coast. As a result, the Sumatra-Java coast constitutes a part of the western Pacific warm pool. Consequently, the climatological mean center of convection is also situated too far west. This center moves eastward and westward with the model ENSO cycle. This is why the ENSO-Australian rainfall teleconnection has the strongest impact in NWA but not eastern Australia in the model (Fig. 13a); this is also why the IOD-like pattern in the Indian Ocean is strongest in DJF. Westward from the warm pool, easterlies superimpose on climatological westerlies to generate general warming as in the observed. Further, as will be clear, there is also a part of the east-west movement of the warm pool that occurs independent of ENSO, and this is reflected in a mode of IOD-like variability after removing the ENSO signals. The main point is that this unrealistic cold tongue structure creates a spurious relationship between SST in the EIO and NWA in DJF, in which an EIO SST increase is associated with an increase in NWA rainfall, a relationship not seen in the observed.

4.1c Seasonal correlation between NWA rainfall with EIO SST and Nino3.4.

The unrealistic feature seen above re-emerges in the ENSO-Australian rainfall relationship (Fig. 14, left column). The unrealistically strong ENSO influence over NWA rainfall is accompanied by a lack of an ENSO signal over eastern Australian rainfall (Fig. 14, left column). This is consistent with the feature of a modeled Pacific warm pool being situated too far west and into the eastern Indian Ocean. In MAM the correlation pattern with ENSO improves over the eastern and southeastern regions, however over NWA, it is far too strong. The pattern in JJA best resembles the observed; however in SON the model completely misses the teleconnection over northern Australia.

In terms of an EIO SST-Australian rainfall relationship (Fig. 14, right column), the correlation pattern in DJF and MAM is virtually the mirror image of that associated with ENSO, suggesting a tight linkage between Nino3.4 and EIO SST in these two seasons, and again reflecting the feature that the EIO is a part of the Pacific warm pool. Similarly, the correlation pattern in JJA compares well with the observed, but in SON the EIO SST influence on northern Australia is underestimated. Most relevant to the present study is

that in DJF, in which the model generates a rainfall increasing trend as in the observed, the model produces a spurious teleconnection in which NWA rainfall is unrealistically influenced by model ENSO. Therefore, an increasing EIO SST is associated with an increase in NWA rainfall in DJF, opposite to that seen in the observed.

4.2 Variability of DJF rainfall

4.2a EOF of DJF SST in the Indian Ocean

As discussed in section 3.2, there is no observed mode of DJF SST variability in the Indian Ocean that dominates the NWA DJF rainfall. In the model, however, there is, i.e., the model ENSO and the associated SST in the EIO are a part of the unrealistic model warm pool (Fig. 13a). In fact, EOF analysis on Indian Ocean SST anomalies in all seasons generates an IOD-like variability pattern, and in DJF the pole in the EIO has the strongest variance. Correlation between the time series of the DJF SST EOF1 and Australian rainfall yields a pattern virtually identical to that shown in Fig. 14a. For DJF, the second EOF resembles the observed second EOF with a pattern reminiscent of that shown in Fig. 7b. We will discuss this later.

To further highlight the unrealistic model ENSO feature, Fig. 15 shows the pattern obtained from regressing SST and surface wind onto a model Nino3.4 index. Compared with the observed (Fig. 5), there is an overall westward shift of the western Pacific anomalies in the model; the model easterlies extend too far into the western Indian Ocean. In association, east of 110°E along the Sumatra-Java coast, the model shows westerlies that extend to the western Pacific rather than the observed easterly anomalies. More importantly, there is strong cooling off the Sumatra-Java coast as the warm pool shifts eastward, and the variability pattern is IOD-like in the Indian Ocean domain.

It happens that after removing the model ENSO, there is an IOD-like mode that operates in DJF. This is realized by conducting EOF analysis on the residual after removing anomalies associated with model Nino3.4, in the tropical Indian Ocean domain. This mode accounts for 22.4%, and has an anomaly pattern (Fig. 15b) that resembles what is

shown in Fig. 15a for the Indian Ocean. This is associated with the movements of the warm pool that is independent from ENSO. This is another unrealistic feature of the model. This mode also has a sizeable correlation with NWA rainfall in the DJF season (Fig. 15c). Indeed a strong correlation is achieved over NWA, significant at 95% confidence level.

4.2b Rainfall EOF in DJF without ENSO and IOD

Given that only about one quarter of the NWA rainfall variance is explained by the model ENSO and that only a small portion (about 5%) is associated with IOD-like variability independent from ENSO, it is appropriate to examine the process that generates the remaining variation. To this end, we remove the variance associated with ENSO (Fig. 15a) and IOD (Fig. 15b) and apply EOF analysis to the residual rainfall following the procedure described in section 3.2. EOF1 (Fig. 16a), which accounts for 16.8% of the total variance, is similar to the observed EOF1 (Fig. 6a), and reflects a feature of a northern-concentration of variance, with little anomalies south of 28°S. EOF2 (Fig. 16b), which generally resembles the observed rainfall EOF2 (Fig. 6b), shows coherence between east and west of 130°E; the east has strong anomalies in the north, and the west shows strong anomalies between 112°E-125°E, 18°S-26°S. Thus even though the model produces several unrealistic features, it still captures important features of NWA rainfall variability.

4.2c Circulation pattern associated with DJF rainfall EOFs

To obtain the SST pattern associated with the rainfall EOF shown in Fig. 16, we regress grid-point SST anomalies onto the two EOF time series (Fig. 17). The regression pattern for EOF1 (Fig. 17a) is generally similar to that associated with the observed rainfall EOF1 without ENSO (Fig. 7a) in terms of enhanced east-west SST gradients towards the WA coast, although the location of maximum anomalies is somewhat different. The SST anomaly pattern associated with EOF2 (Fig. 17b) is also similar to that shown in Fig. 7b with warming anomalies over much of NWA. The circulation pattern in terms of SLP,

surface winds, and cloud cover are similarly obtained (Figs. 18a and 18b, and Figs. 19a and 19b). Despite the model's absence in the model of a strong subtropical high pressure anomaly center, which is rather prominent in the observed (Fig. 8a), the results generally support the notion that similar dynamical processes operate in the model. Associated with the rainfall EOF1 is a cyclonic flow pattern centered off NWA with northerlies advecting high moisture air mass to northern Australia (Fig. 18a), contributing to the high rainfall, with consistently higher cloud cover (Fig. 19a). By contrast, an anticyclonic pattern is associated with EOF2, with anomalously high MSLP over Australia with northwesterlies west of 130°E picking up moist air before impinging on the WA coast; east of 130°E, there are southerly anomalies to the north and decreased cloud. Thus it seems that, except for the unrealistic ENSO and IOD-like patterns and the associated unrealistic rainfall teleconnection, the model does realistically capture the dynamical mechanisms as revealed in the observations.

However, these two modes appear to be weaker than the observed. Comparing Figs. 18, 19 with 7, 8, we see that the model anomalies are approximately half of observed; similarly, the model MSLP and wind stress anomalies are also much weaker.

4.3 The dynamics of DJF model rainfall trend in the presence of increasing aerosols

We now attribute how much of the model DJF rainfall increase (Fig. 12a) is attributable to the DJF rainfall (Fig. 16) trend in ENSO (Fig. 15). To this end, we project raw DJF rainfall outputs from the ALL ensemble onto the two EOF patterns for each year from 1951 to 2000. A time series of pattern regressions for each mode is obtained and the trend is calculated. Multiplying the total trend in the time series with the EOF patterns gives the trend associated with EOF1 and EOF2. We find that there is little trend embedded in the two EOFs; their sum accounts for less than 10% of the total trend.

Similarly, we project SST outputs from the ALL ensemble onto the model ENSO pattern (Fig. 15) to obtain a time series of pattern regression coefficients, from which the total trend is obtained. Separately, we regress the control DJF rainfall onto the control Nino3.4

to obtain a regression pattern, which describes how rainfall varies with ENSO. The pattern is similar to that shown in Fig. 12a. Multiplying the total trend in the time series with the regression pattern gives the trend map associated with ENSO. We find that the increasing rainfall trend in this set of experiments is not associated with an ENSO-like trend pattern.

Most of the rainfall trend is attributable to the unrealistic teleconnection of NWA rainfall with the EIO SST in this season, embedded in the control run, as shown in Fig. 14e. Regressing grid-point DJF rainfall anomalies onto the time series of DJF SST in the EIO (90°E - 110°E , 5°S - 15°S) in the control run yields a map of a regression pattern, $G(x,y)_{control}$, similar to that shown in Fig. 14e describing the relationship between Australian rainfall and the EIO SST. In the presence of the aerosol forcing, there is an increase in the EIO SST incorporated in an IOD-like trend pattern (Fig. 20a). There are indeed increased SST gradients toward WA, but they are weaker than the observed. More importantly, the pattern is overwhelmed by the large increase in SST off the Sumatra-Java coast. The trend of a time series of DJF SST over the EIO box in the ALL ensemble, $\nabla f(t)_{All}$, is calculated, multiplying $\nabla f(t)_{All}$ with the regression pattern $G(x,y)_{control}$ and this generates a total trend that is due to the unrealistic model relationship of EIO SST with Australian rainfall (Fig. 20b). Comparing with Fig. 12e, we see a good agreement, supporting that most of the DJF rainfall increasing trend in the ALL ensemble is caused by the unrealistic teleconnection in the model.

The process that leads to the increase in the EIO SST has been explored in Rotstayn et al. (2007). In brief, the north-south thermal gradient (cooler in the Northern Hemisphere) cause changes in the surface winds, which tend to flow from the cooler equatorial to the southern tropical regions, but are deflected to the left such that along the Sumatra-Java coast trend of northwesterlies is generated, depressing the thermocline and generating the warming, accompanied by an increasing rainfall trend over the EIO, extending into the NWA.

5. Conclusions and discussion

Since 1950, eastern Australia and southwest WA has experienced decreasing rainfall trends. An exception is NWA, where a substantial increasing trend is observed. A recent study using 20th century multi-member ensemble simulations in a global climate model forced with and without increasing anthropogenic aerosol forcing (Rotstayn et al. 2007) suggests that the increasing rainfall trend over NWA is attributable to the increasing Northern Hemispheric aerosols. The present study investigates the dynamics of the observed trend and compares with that seen in a climate model. We benchmark the model results in terms of drivers of NWA rainfall variability for each season, and examine the possibility that the increasing rainfall trend projects onto existing modes of variability.

We find that the observed rainfall variability over NWA is weakly correlated with ENSO in all seasons, and features a weak increase during a La Niña event, and vice versa during El Niño. In JJA and SON, NWA rainfall is influenced by IOD variability with an increased SST in the EIO linked to an increase in NWA rainfall. In DJF, NWA rainfall tends to increase when a La Niña event generates basin-scaled cooling but with increased SST gradients towards the NWA coast. In this way, a decreased EIO SST in DJF is associated with an increased NWA rainfall. The reverse occurs during an El Niño event. The SST trend over the past 50 years shows an El Niño-like pattern in the Indo-Pacific system, therefore it is unable to explain the increasing rainfall trend over NWA. Indeed, without the impact of the El Niño-like pattern, rainfall increase is greater.

The observed rainfall increase occurs in the DJF season and is projected onto two modes of variability. The first mode is associated with an anomalously low MSLP off the NWA and WA coast instigated by the enhanced SST gradients towards the coast. The associated cyclonic flows bring high moisture air to northern Australia, thus leading to an increase in rainfall. The second mode is associated with anomalously high MSLP over much of the Australian continent; the anticyclonic circulation pattern with northwesterly flows west of 130°E and generally opposite flows in northeast Australia, determine that

rainfall variability west and east of 130°E is of opposite polarity with anomalously high rainfall to the west and anomalously low rainfall to the east. The sum of the upward trend in these two modes generates the trend pattern with increasing NWA rainfall as shown in Fig. 1.

The total SST trend associated with the two EOFs resembles that of the raw SST in the sense that both show increased gradients towards the NWA coast. It is not clear what drives the increased SST gradient along the coast. An enhanced Leeuwin Current with intensified onshore flows would be consistent with this change in the SST gradient. However, the Leeuwin Current is strongest in the Southern Hemisphere winter and is strongly correlated with ENSO, with a weakening current during an El Niño event. Over the past 50 years an El Niño-like pattern has featured strongly in the Pacific which would mean a weakening Leeuwin Current. A detailed study on the dynamics of the increased east-west gradients toward the coast is beyond the scope of the present study.

In the presence of aerosol forcing, the ensemble mean generates a realistic seasonal trend. As in the observed, the model rainfall increase occurs in the DJF season. Further, in the corresponding control experiment (no external forcing), modes of NWA rainfall variability resemble the observed after removing the unrealistic features associated with model ENSO and variability over the Indian Ocean. However, the model rainfall trend appears to be generated by processes that are not operating in the real climate system. As in other models, our model suffers from an equatorial cold-tongue bias: the tongue of anomalies associated with ENSO extends too far west into the western Pacific.

Indeed the model anomaly tongue extends to the EIO with several ensuing consequences. Firstly, as the position of the warm pool moves in the zonal direction with the model ENSO-like events, the strongest Australian rainfall-ENSO teleconnection lies in NWA, rather than the observed northeastern Australia. Secondly, in all seasons, the Indian Ocean has an IOD-like variability pattern; in DJF, apart from an IOD-like pattern that is linked with ENSO, there is also an IOD-like pattern that is independent from ENSO;

neither is realistic as the observed IOD only takes place in the JJA and SON seasons. This unrealistic presence of IOD-like variability in DJF generates an unrealistic EIO SST-NWA rainfall relationship, with an increasing SST in the EIO being associated with increasing NWA rainfall. In the observations such a relationship does not exist.

In the presence of increasing aerosols, a significant SST increase occurs in the tropical EIO with an overall pattern resembling the negative IOD phase. As a result, the modeled rainfall increase can be accounted for by the unrealistic relationship between model EIO SST and NWA rainfall that operates in the control experiment. This unrealistic relationship results from the model cold tongue problem. It is not clear if a model without such defects will produce the observed rainfall trend under forcing of increasing aerosols. Further modeling studies are therefore needed to properly evaluate the impact of aerosols on Australian rainfall.

Acknowledgement

We thank the three reviewers for their helpful comments. CSIRO scientists are also supported by the Australian Greenhouse Office.

Reference

Ashok, K., Z. Guan, and T. Yamagata, 2003: Influence of the Indian Ocean Dipole on the Australian winter rainfall, *Geophys. Res. Lett.*, **30**, 1821, doi:10.1029/2003GL017926.

Ashok, K., H. Nakamura and T. Yamagata, 2007a: Impacts of ENSO and Indian Ocean Dipole events on the southern hemisphere storm track activity during austral winter, *J. Clim.*, in press.

Ashok, K., S. K. Behera, S. A. Rao, H. Weng and T. Yamagata, 2007b: El Niño Modoki and its teleconnection, *J. Geophys. Res.*, in press

Cai, W., and T. Cowan, 2006: SAM and regional rainfall in IPCC AR4 models: Can anthropogenic forcing account for southwest western Australian winter rainfall reduction? *Geophys. Res. Lett.*, **33**, L24708, doi:10.1029/2006GL028037.

Cai, W., H. H. Hendon, and G. Meyers, 2005a: Indian Ocean Dipolelike Variability in the CSIRO Mark 3 Coupled Climate Model. *J. Clim.*, **18**, 1449–1468.

Cai, W., G. Shi, and Y. Li, 2005b: Multidecadal fluctuations of winter rainfall over southwest Western Australia simulated in the CSIRO Mark 3 coupled model, *Geophys. Res. Lett.*, **32**, L12701, doi: 10.1029/2005GL022712.

Cai, W., and P. H. Whetton, 2000: Evidence for a time-varying pattern of greenhouse warming in the Pacific Ocean, *Geophys. Res. Lett.*, **27**, 2577–2580.

Cai, W. J., P. H. Whetton, and D. J. Karoly, 2003: The response of the Antarctic Oscillation to increasing and stabilized atmospheric CO₂. *J. Climate*, **16** (10): 1525–1538.

Chambers, D. P., B. D. Tapley, and R. H. Stewart, 1999: Anomalous warming in the Indian Ocean coincident with El Niño. *J. Geophys. Res.*, **104**, 3035–3047.

Clarke, G. K. C., H. L. Treut, R. S. Lindzen, V. P. Meleshko, R. K. Mugara, T. N. Palmer, R. T. Pierrehumbert, P. J. Sellers, and J.W. K. E. Trenberth, 2001: Physical climate processes and feedbacks, in *Climate Change 2001: The Scientific Basis. Contribution of Working Group I to the Third Assessment Report of the Intergovernmental Panel on Climate Change (IPCC)*, edited by J. T. Houghton, Y. Ding, D. J. Griggs, M. Noguer, P. J. van der Linden, X. Dai, K. Maskell, and C. A. Johnson, Cambridge Univ. Press, Cambridge, United Kingdom, 417–470.

Cubasch, U., G. A. Meehl, G. J. Boer, R. J. Stouffer, M. Dix, A. Noda, C. A. Senior, S. Raper, and K. S. Yap, 2001: Projections of future climate change. In: Houghton, J.T., Ding, Y., Griggs, D.J., Noguer, M., van der Linden, P., Dai, X., Maskell, K. and Johnson, C.I. (Eds.). *Climate Change 2001: The Scientific Basis. Contribution of Working Group I*

to the 3rd Assessment Report of the Intergovernmental Panel on Climate Change. Cambridge University Press, Cambridge, UK, pp. 525-582.

England, M. H., C. C. Ummenhofer, and A. S. Santoso, 2006: Interannual rainfall extremes over Southwest Western Australia linked to Indian Ocean climate variability, *J. Climate*, **19**, 1948–1969, DOI: 10.1175/JCLI3700.1.

Fyfe, J. C., G. J. Boer, and G. M. Flato, 1999: The Arctic and Antarctic Oscillations and their projected changes under global warming. *Geophys. Res. Lett.*, **26**, 1601–1604.

Feng, M., and G. Meyers, 2003: Interannual variability in the tropical Indian Ocean: A two-year time scale of Indian Ocean Dipole. *Deep-Sea Res.*, **50**, 2263–2284.

Hartmann, D. L., and F. Lo, 1998: Wave-driven zonal flow vacillation in the Southern Hemisphere. *J. Atmos. Sci.*, **55**, 1303–1315.

Hendon, H. H., D. W. J. Thompson, and M. C. Wheeler, 2006: Australian rainfall and surface temperature variations associated with the Southern Hemisphere Annular Mode. *J. Clim.* (submitted).

Kalnay, E., M. Kanamitsu, R. Kistler, W. Collins, D. Deaven, L. Gandin, M. Iredell, S. Saha, G. White, J. Woolen, Y. Zhu, M. Chelliah, W. Ebisuzaki, W. Higgins, J. Janowiak, K. C. Mo, C. Ropelewski, J. Wang, A. Leetma, R. Reynolds, R. Jenne, and D. Joseph, 1996: The NCEP/NCAR 40-year reanalysis project. *Bullet. Amer. Meteorol. Soc.*, **77**, 437-471.

Karoly, D. J., 1990: The role of transient eddies in low-frequency zonal variations of the Southern Hemisphere circulation. *Tellus*, **42A**, 41–50.

Kidson, J. W., 1988: Interannual variations in the Southern Hemisphere circulation. *J. Clim.*, **1**, 1177–1198.

Klein, S. A., B. J. Soden, and N.-C. Lau, 1999: Evidence for a tropical atmospheric bridge. *J. Clim.*, **12**, 917–932.

Kushner, P. J., I. M. Held, and T. L. Delworth, 2001: Southern Hemisphere atmospheric circulation response to global warming. *J. Clim.*, **14**, 2238-2249.

Lau, N.-C., and M. J. Nath, 2004: Coupled GCM simulation of atmosphere–ocean variability associated with zonally asymmetric SST changes in the tropical Indian Ocean. *J. Clim.*, **17**, 245–265.

McBride, J.L. and N. Nicholls, 1983: Seasonal relationships between Australian rainfall and the Southern Oscillation. *Mon. Wea. Rev.*, **111**, 1998-2004.

Meehl, G. A., and W. M. Washington, 1995: Cloud albedo feedback and the super greenhouse effect, *Clim. Dyn.*, **11**, 399–411.

Murphy, J. M., and J. F. B. Mitchell, 1995: Transient Response of the Hadley Centre Coupled Ocean-Atmosphere Model to Increasing Carbon Dioxide. Part II: Spatial and Temporal Structure of Response. *J. Clim.*, **8**, 57–80.

Nicholls, N., 1989: Sea surface temperature and Australian winter rainfall. *J. Clim.*, **2**, 965-973.

Pitman, A. J., G. T. Narisma, R.A. Pielke, and N. J. Holbrook, 2004: Impact of land cover change on the climate of southwest Western Australia, *J. Geophys. Res.*, **109**, D18109, doi: 10.1029/2003JD004347.

Rao, S., A., S. K. Behera, Y. Masumoto and T. Yamagata, 2002: Interannual variability in the subsurface Indian Ocean with special emphasis on the Indian Ocean Dipole. 2002 *Deep Sea Res.-II*, **49**, 1549-1572.

Ropelewski, C.F. and M.S. Halpert, 1987: Global and regional scale precipitation patterns associated with El Niño/Southern Oscillation, *Mon. Wea. Rev.*, **115**, 1606-1626.

Ropelewski, C.F. and M.S. Halpert, 1989: Precipitation patterns associated with high index phase of Southern Oscillation, *J. Clim.*, **2**, 268-284.

Rotstayn, L.D., W., Cai, M.R. Dix, G.D. Farquhar, Y. Feng, P. Ginoux, M. Herzog, A. Ito, J.E. Penner, M. L. Roderick, and M. Wang, 2007: Have Australian rainfall and cloudiness increased due to the remote effects of Asian anthropogenic aerosols? *J. Geophys. Res.*, 112, D09202, doi:10.1029/2006JD007712.

Saji, N. H., B. N. Goswami, P. N. Vinayachandran, and T. Yamagata, 1999: A dipole mode in the tropical Indian Ocean, *Nature*, **401**, 360–363.

Saji, N.H., and Yamagata, T., 2003. Possible impacts of Indian Ocean dipole mode events on global climate. *Climate Res.*, **25**, 151-169.

Samuel J. M., D. C. Verdon, M. Sivapalan, S. W. Franks, 2006: Influence of Indian Ocean sea surface temperature variability on southwest Western Australian winter rainfall, *Water Resour. Res.*, **42**, W08402, doi:10.1029/2005WR004672.

Shinoda, T., M. A. Alexander, and H. H. Hendon, 2004: Remote response of the Indian Ocean to SST variations in the tropical Pacific. *J. Clim.*, **17**, 362–372

Smith, I. N., 2004: An assessment of recent trends in Australian rainfall, *Aust. Meteorol. Mag.*, **53**, 163–173.

Stouffer, R. J., S. Manabe, and K. Bryan, 1989: Interhemispheric asymmetry in climate response to a gradual increase of CO₂, *Nature*, **342**, 660-662.

Thompson, D. W. J, J. M. Wallace, and G. C. Hegerl, 2000: Annular modes in the extratropical circulation. Part II: Trends. *J. Clim.*, **13**, 1018–1036.

Verdon D. C., S. W. Franks, 2005: Indian Ocean sea surface temperature variability and winter rainfall: Eastern Australia, *Water Resour. Res.*, **41**, W09413, doi:10.1029/2004WR003845.

Wardle, R., and I. N. Smith, 2004: Modeled response of the Australian monsoon to changes in land surface temperatures, *Geophys. Res. Lett.*, **31**, L16205, doi:10.1029/2004GL020157.

Webster, P. J., A. Moore, J. P. Loschnigg, and R. R. Leben, 1999: Coupled oceanic–atmospheric dynamics in the Indian Ocean during 1997–1998. *Nature*, **401**, 356–360.

Weng, H., K. Ashok, S. K. Behera, S. A. Rao and T. Yamagata, Climate dynamics (published online): Impacts of Recent El Niño Modoki on Dry/Wet Conditions in the Pacific Rim during Boreal Summer, 2007 (available from [http://www.jamstec.go.jp/frsgc/research/d1/iod/.](http://www.jamstec.go.jp/frsgc/research/d1/iod/))

Whetton, P. H., M. H. England, S. P. O’Farrell, I. G. Watterson, and A. B. Pittock, 1996: Global comparison of the regional rainfall results of enhanced greenhouse coupled and mixed layer ocean experiments: Implications for climate change scenario development, *Climatic Change*, **33**, 497–519.

Xie, S., K.-M. Xu, R.T. Cederwall, P. Bechtold, A.D. Del Genio, S.A. Klein, D.G. Cripe, S.J. Ghan, D. Gregory, S.F. Iacobellis, S.K. Krueger, U. Lohmann, J.C. Petch, D.A. Randall, L.D. Rotstain, R.C.J. Somerville, Y.C. Sud, K. von Salzen, G.K. Walker, A. Wolf, J.J. Yio, G.J. Zhang, and M. Zhang, 2002: Intercomparison and evaluation of cumulus parameterizations under summertime midlatitude continental conditions. *Q. J. Royal Meteor. Soc.* **128**, 1095-1136.

Yamagata, T., S. K. Behera, J.J. Luo, S. Masson, M. R. Jury, and S. A. Rao, 2004: Coupled Ocean-Atmosphere variability in the Tropical Indian Ocean, *Earth's climate: The Ocean-Atmosphere Interaction Geophysical Monograph Series*. **147**, doi:10.1029/147GM12, Eds. by Wang, C., S.-P. Xie, and J.A. Carton.

Yoo S.-H., S. Yang, C.-H. Ho (2006), Variability of the Indian Ocean sea surface temperature and its impacts on Asian-Australian monsoon climate, *J. Geophys. Res.*, **111**, D03108, doi:10.1029/2005JD006001.

Figure Captions

Figure 1: Observed annual total rainfall trend (mm) based on the BMRC rainfall data over 1951-2000. Blue colour shows rainfall increase and red indicates rainfall reduction. The area in the Northwest corner (dotted line) is defined as NWA in this paper.

Figure 2: Observed climatology (left column) and trend (right column) of seasonal total rainfall (mm) over 1951-2000. The data are stratified into December-January-February (DJF), March-April-May (MAM), June-July-August (JJA), and September-October-November (SON).

Figure 3: Map of correlation between NWA rainfall and grid-point SST (both linearly detrended) for each season using data for the 1951-2000 period. Correlation coefficients greater than 0.28 are significant at a 95% confidence level.

Figure 4: Maps of correlation of Australian rainfall with Nino3.4 ($^{\circ}\text{C}$, left column) and with EIO SST (right column) for each season using data for the 1951-2000 period.

Figure 5: Patterns of SST (GISST, in $^{\circ}\text{C } ^{\circ}\text{C}^{-1}$) and wind (NCEP, maximum vector $0.02 \text{ N m}^{-2} ^{\circ}\text{C}^{-1}$) anomalies associated with ENSO. These are obtained by regressing linearly detrended SST and wind fields onto linearly detrended Nino3.4.

Figure 6: Patterns associated with detrended rainfall EOF after removing variances associated with ENSO (see text for details) in the domain of 110°E-135°E, 10°S-25°S. These patterns are obtained by regressing grid-point Australia rainfall anomalies onto the time series of the EOF1 and EOF2.

Figure 7: SST patterns associated with EOF1 and EOF2 shown in Fig. 6. Shown are obtained by regressing SST anomalies onto the time series of the EOF1 and EOF2. Units are in °C per unit of the EOF time series.

Figure 8: Anomaly patterns of MSLP (mb per unit of EOF time series) and winds (N m^{-2} per unit of EOF time series) associated with EOF1 and EOF2 shown in Fig. 6. Shown are obtained by regressing anomalies onto the rainfall time series of the EOF1 and EOF2. The regression coefficients of surface winds are plotted as vectors.

Figure 9: The same as Fig. 8, but for cloud cover.

Figure 10: DJF total rainfall trends (mm) projected onto EOF1 (a) and EOF2 (b), and the sum of them (c). Since these trends are obtained by projecting onto DJF rainfall with variance associated with ENSO removal, the ENSO related trend is generated and added to (c) to yield (d).

Figure 11: Panel a), SST trend (°C) resulting from the sum of trends associated with DJF rainfall EOF1 and EOF2 of DJF rainfall shown in Fig.6. These trends are calculated by projecting raw DJF SST anomalies onto time series of the DJF rainfall EOFs (see text for details). Panel b), the total trend of raw SST. Panels c) and d), the same as a) and b) except for MSLP. A uniform value 0.35°C is taken out from b) and a value of 1.4 mb is subtracted from d), respectively.

Figure 12: Model climatology (left column) from a 300-year control experiment of seasonal total rainfall (mm) and trend (right column) in seasonal total rainfall (mm) for 1951-2000.. The data are stratified into December-January-February (DJF), March-April-

May (MAM), June-July-August (JJA), and September-October-November (SON).

Figure 13: Map of correlation between modeled NWA rainfall and model grid-point SST (both linearly detrended) for each season using outputs from a 300-year control experiment. Correlation coefficients greater than 0.12 are significant at a 95% confidence level.

Figure 14: Maps of correlation of Australian rainfall with Nino3.4 (left column) and with EIO SST (right column) for each season using outputs from a 300-year control experiment model outputs.

Figure 15: Panel a), pattern of model SST ($^{\circ}\text{C } ^{\circ}\text{C}^{-1}$, contour) and wind ($\text{N m}^{-2} \text{ } ^{\circ}\text{C}^{-1}$, vectors) anomalies associated with model ENSO-like variability. These are obtained by regressing model SST and wind anomalies onto the model Nino3.4 index in the 300-year control experiment. Panel b), EOF2 (16.8% of the remaining variance) of model SST and the associated model wind fields (vectors) after removing variance associated with ENSO-like variability, and c), correlation between time series of model EOF2 shown in b) and model rainfall.

Figure 16: Patterns of model rainfall EOF after removing variances associated with ENSO and IOD (see text for details). Patterns are obtained by regressing rainfall anomalies onto the time series of the model EOF1 and EOF2 in the domain of 110°E - 135°E , 10°S - 25°S . EOFs 1 and 2 account for 47.6% and 20.7% of the remaining anomalies.

Figure 17: SST patterns associated with model rainfall EOF1 and EOF2 shown in Fig. 16. Patterns are obtained by regressing model SST anomalies onto the time series of the EOF1 and EOF2. Units are in $^{\circ}\text{C}$ per unit of the EOF time series.

Figure 18: Anomaly patterns of MSLP (mb per unit of EOF time series) and winds (N

m^{-2} per unit of EOF time series) associated with DJF rainfall EOF1 and EOF2 in the 300-year control experiment. Patterns are obtained by regressing model MSLP anomalies onto the time series of the rainfall EOFs.

Figure 19: As in Figure 18, but for the cloud cover.

Figure 20: Panel a), model DJF SST trend pattern ($^{\circ}\text{C}$) with all forcing imposed (ALL ensemble). Panel b), total trend (mm) of the DJF rainfall estimated from the unrealistic relationship between EIO SST and Australian rainfall in the 300-year control experiment.

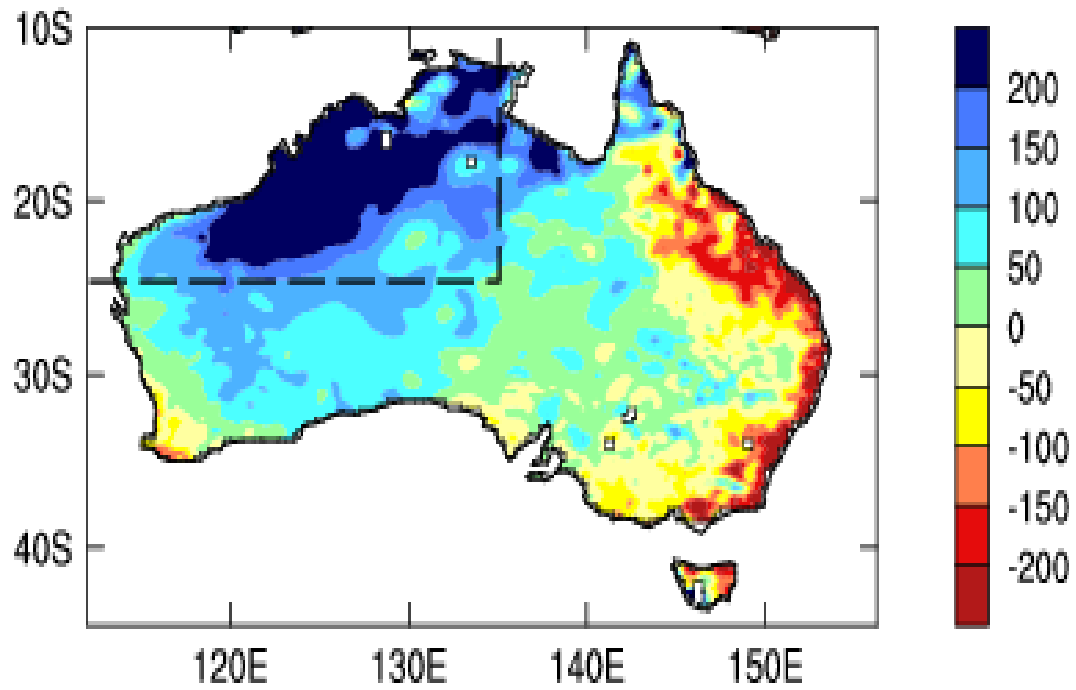


Figure 1: Observed annual total rainfall trend (mm) based on the BMRC rainfall data over 1951-2000. Blue colour shows rainfall increase and red indicates rainfall reduction. The area in the Northwest corner (dotted line) is defined as NWA in this paper.

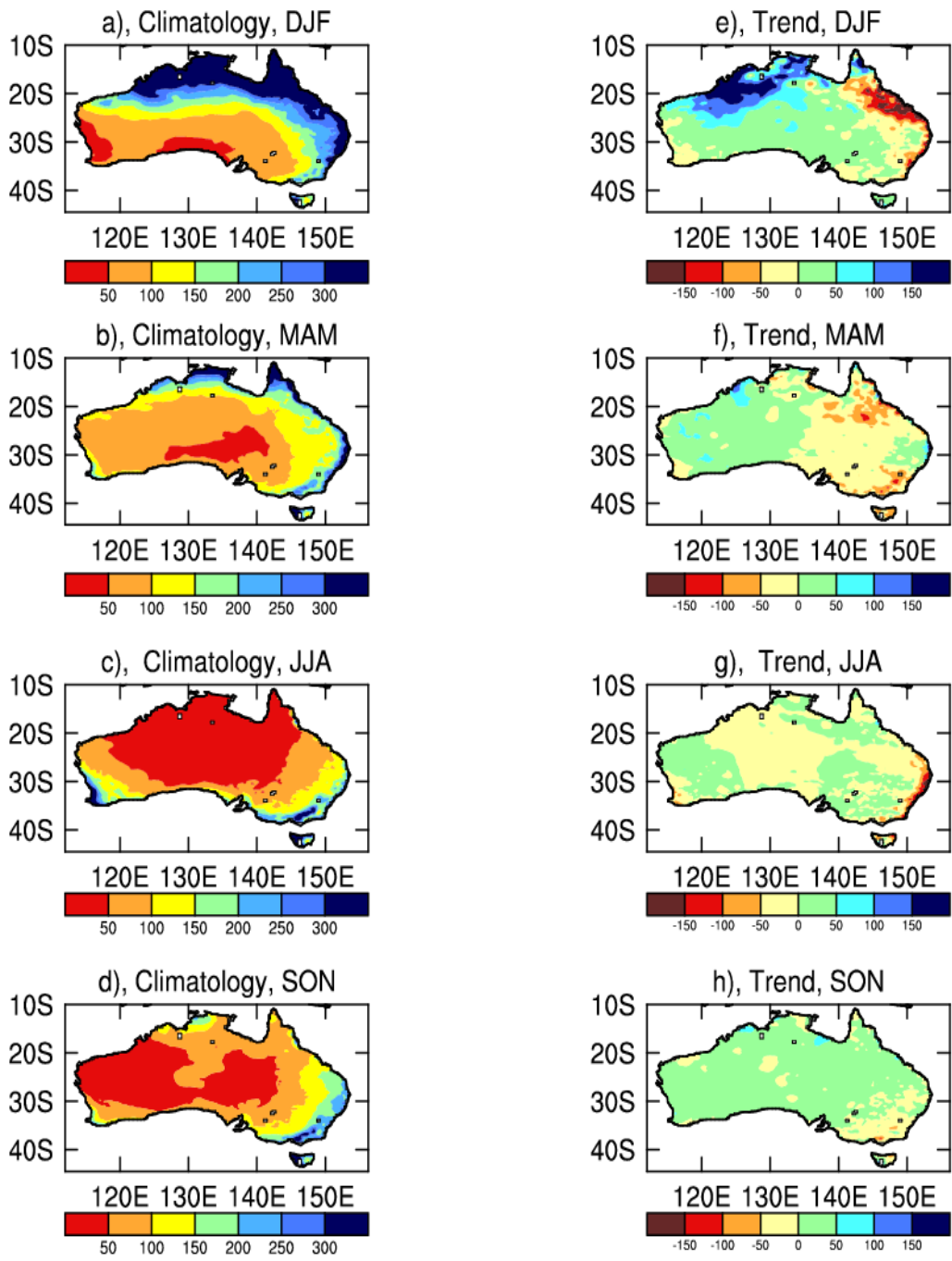


Figure 2: Observed climatology (left column) and trend (right column) of seasonal total rainfall (mm) over 1951-2000. The data are stratified into December-January-February (DJF), March-April-May (MAM), June-July-August (JJA), and September-October-November (SON).

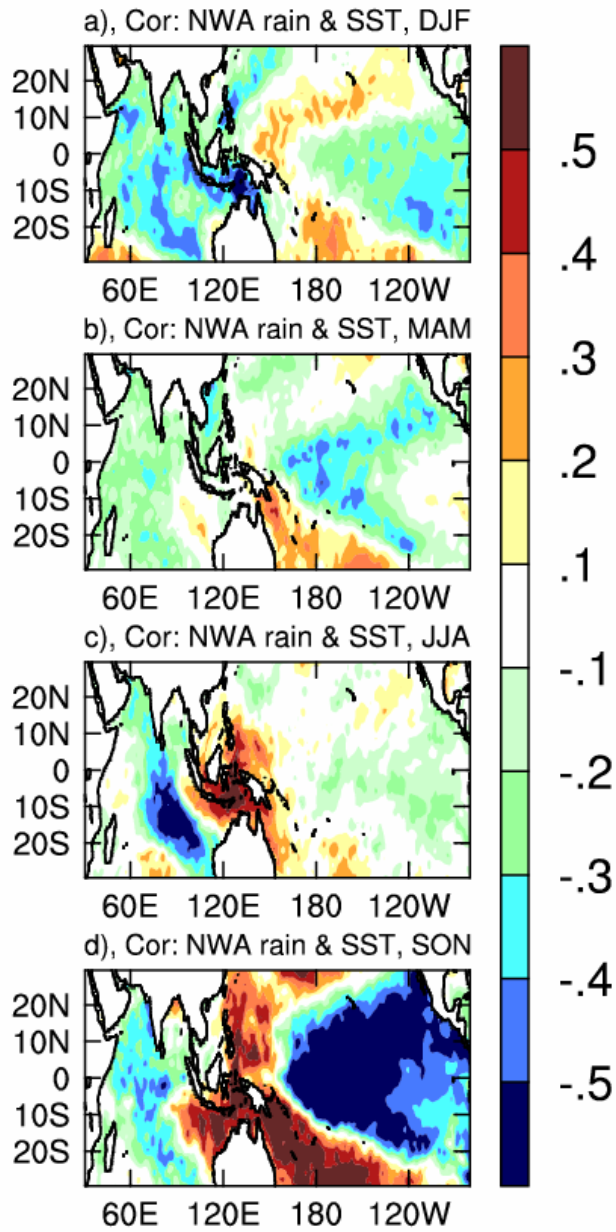


Figure 3: Map of correlation between NWA rainfall and grid-point SST (both linearly detrended) for each season using data for the 1951-2000 period. Correlation coefficients greater than 0.28 are significant at a 95% confidence level.

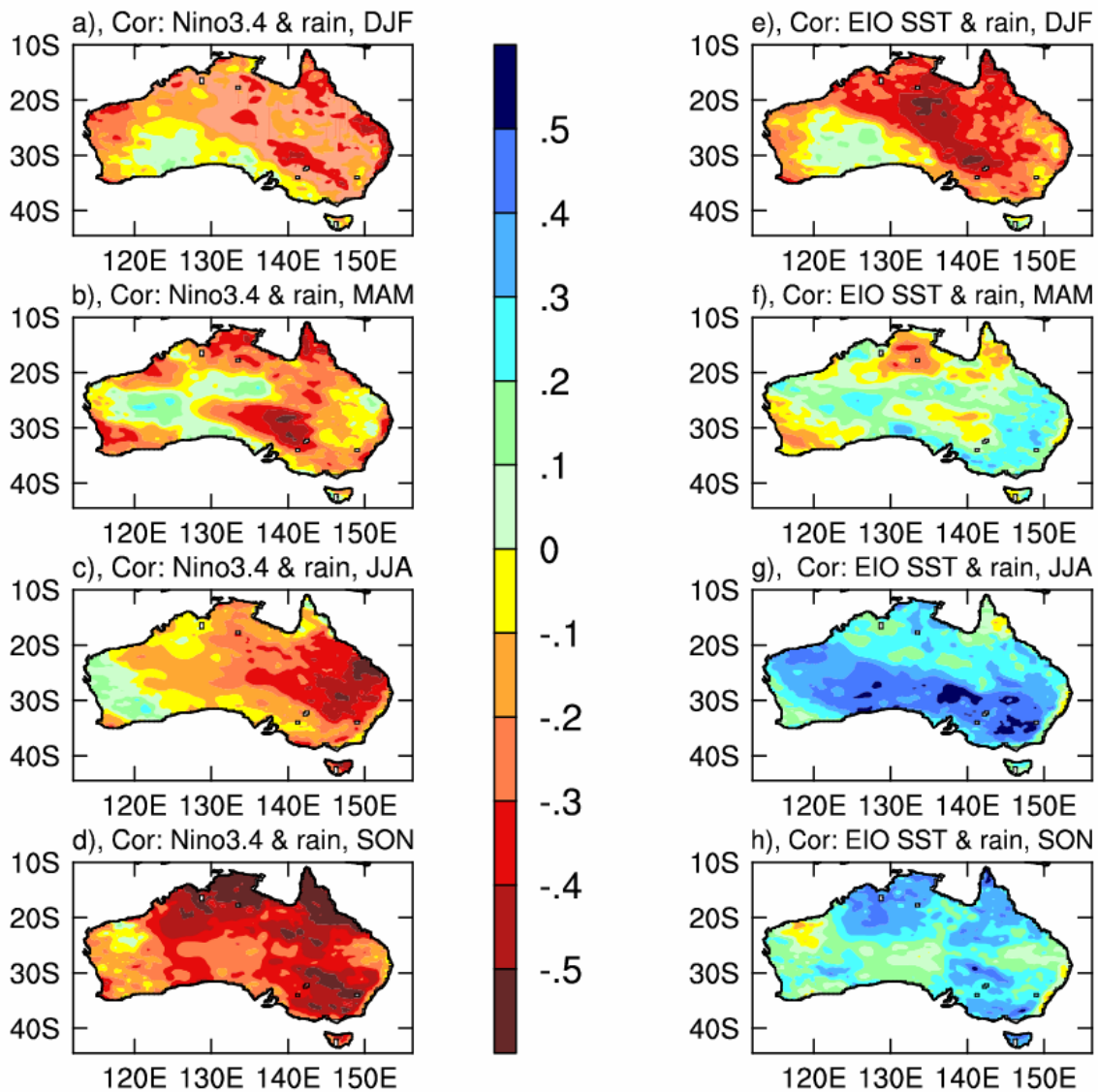


Figure 4: Maps of correlation of Australian rainfall with Nino3.4 (left column) and with EIO SST (right column) for each season using data for the 1951-2000 period.

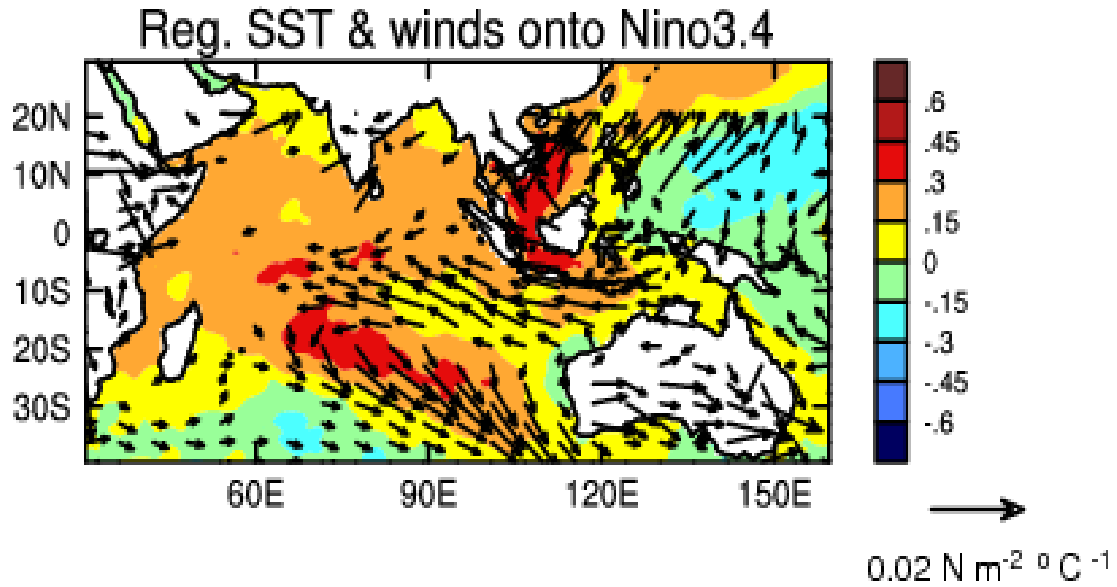


Figure 5: Patterns of SST (GISST, in $^\circ\text{C } ^\circ\text{C}^{-1}$) and wind (NCEP, maximum vector 0.02 $\text{N m}^{-2} \text{ } ^\circ\text{C}^{-1}$) anomalies associated with ENSO. These are obtained by regressing linearly detrended SST and wind fields onto linearly detrended Nino3.4.

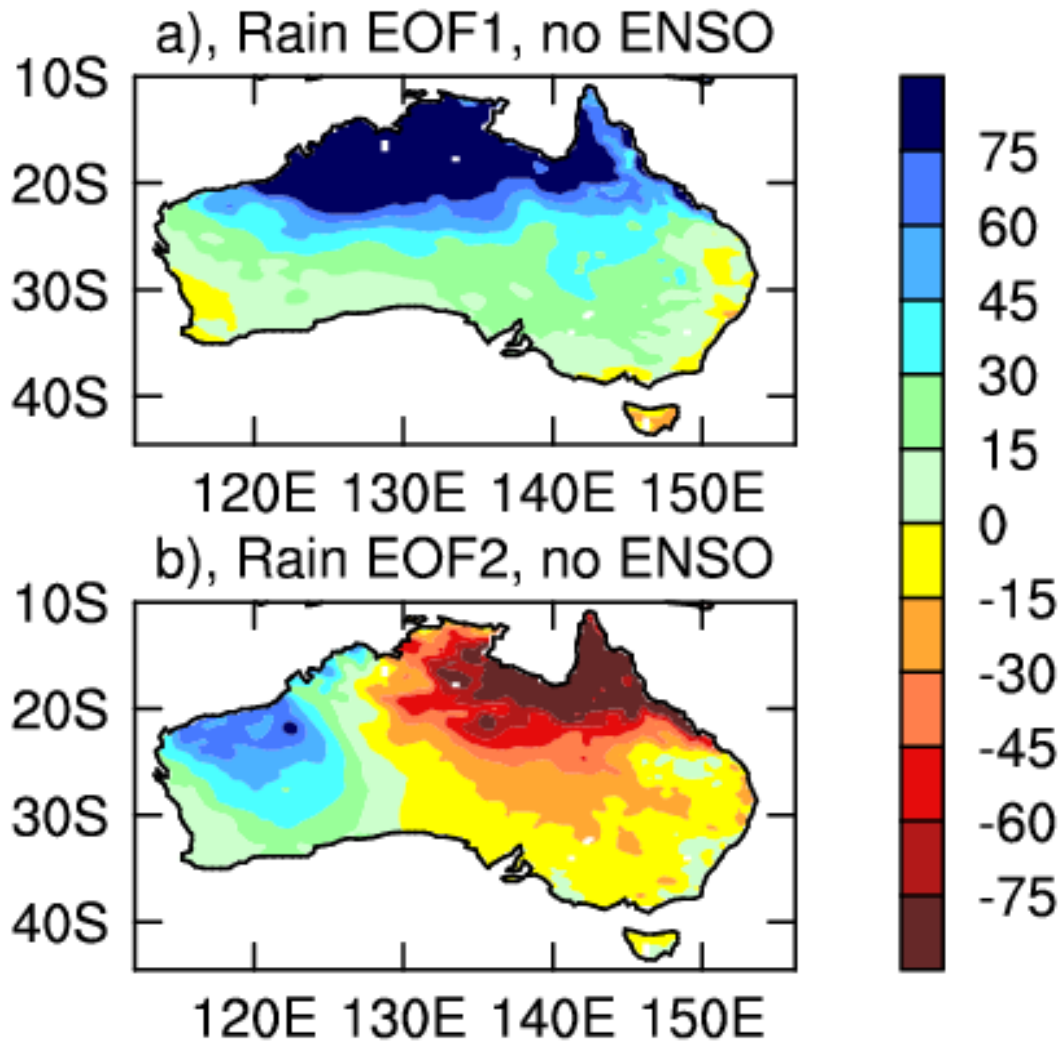


Figure 6: Patterns associated with detrended DJF rainfall EOF after removing variances associated with ENSO (see text for details) in the domain of 110°E-135°E, 10°S-25°S. These patterns are obtained by regressing grid-point Australia rainfall anomalies onto the time series of the EOF1 and EOF2.

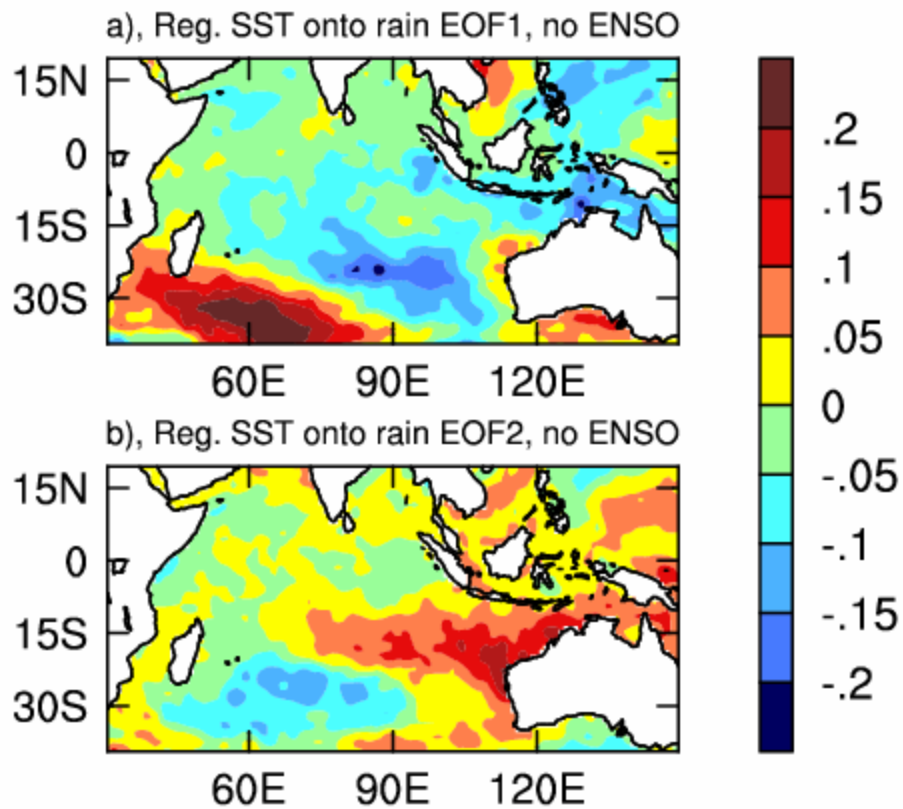


Figure 7: SST patterns associated with EOF1 and EOF2 shown in Fig. 6. Shown are obtained by regressing SST anomalies onto the time series of the EOF1 and EOF2. Units are $^{\circ}\text{C}$ per unit of the EOF time series.

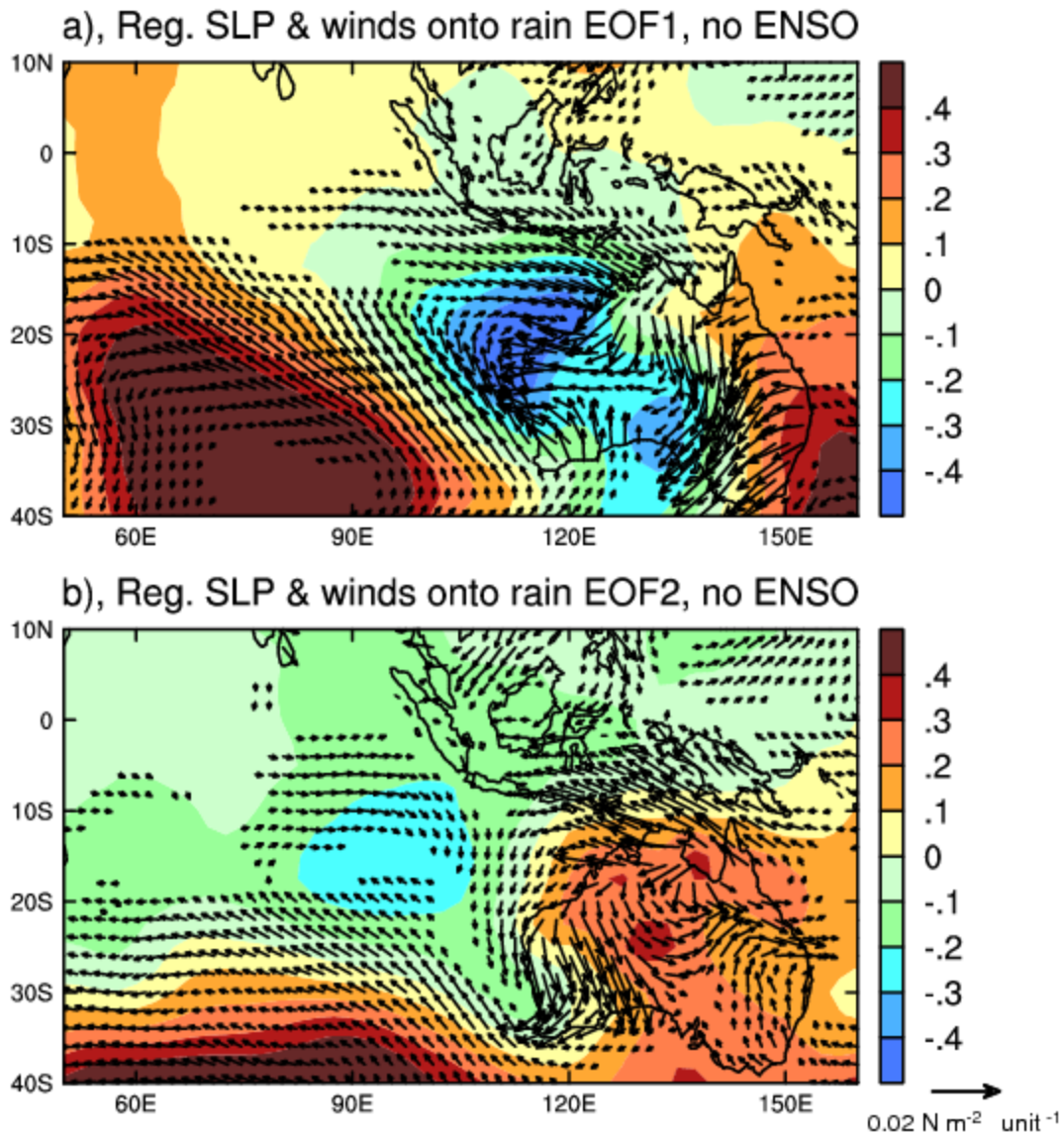
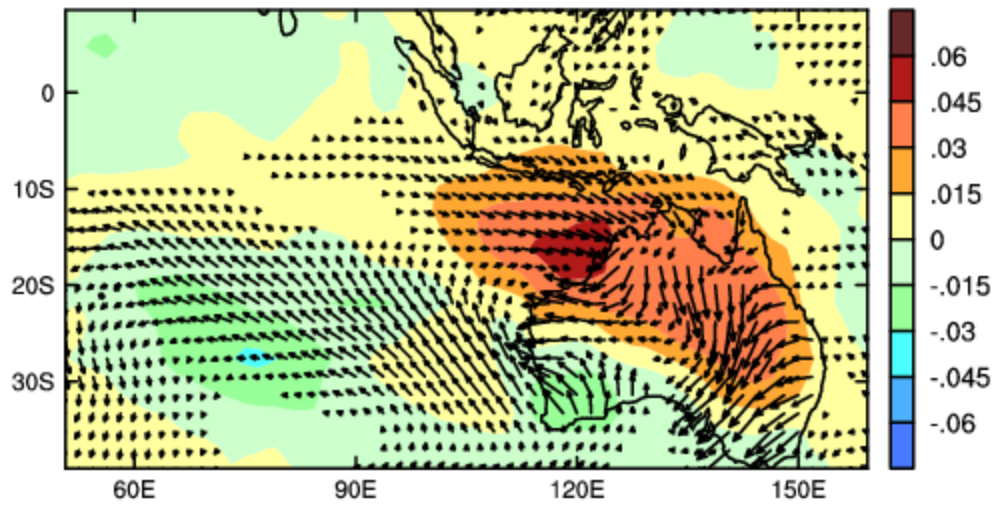


Figure 8: Anomaly patterns of MSLP (mb per unit of EOF time series) and winds (N m⁻² per unit of EOF time series) associated with EOF1 and EOF2 shown in Fig. 6. Shown are obtained by regressing anomalies onto the rainfall time series of the EOF1 and EOF2. The regression coefficients of surface winds are plotted as vectors.

a), Reg. cloud & winds onto no-ENSO rain EOF1



b), Reg. cloud & winds onto no-ENSO rain EOF2

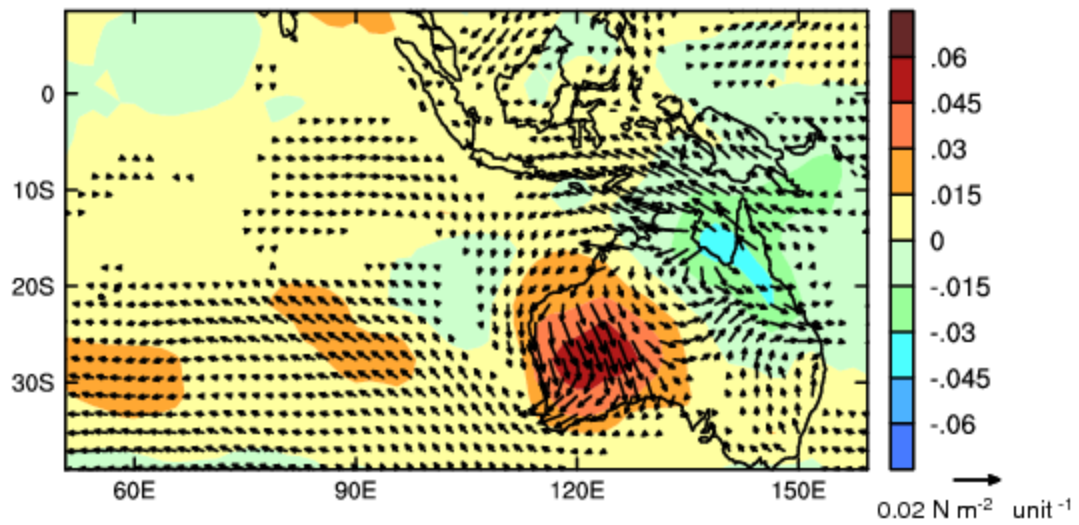


Figure 9: The same as Fig. 8, but for cloud cover.

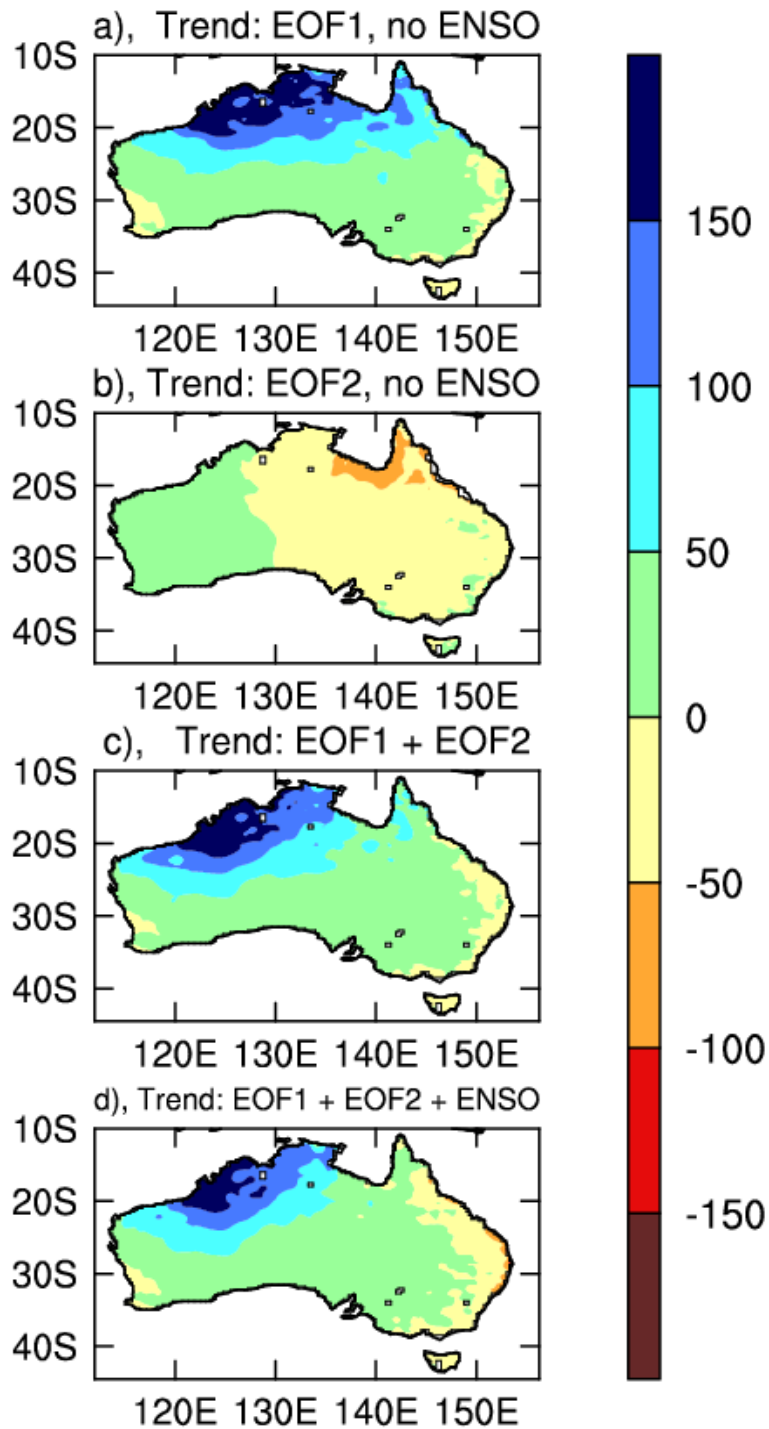


Figure 10: DJF total rainfall trends (mm) over 1951-2000 projected onto EOF1 (a) and EOF2 (b), and the sum of them (c). Since these trends are obtained by projecting onto DJF rainfall with variance associated with ENSO removal, the ENSO related trend is generated and added to (c) to yield (d).

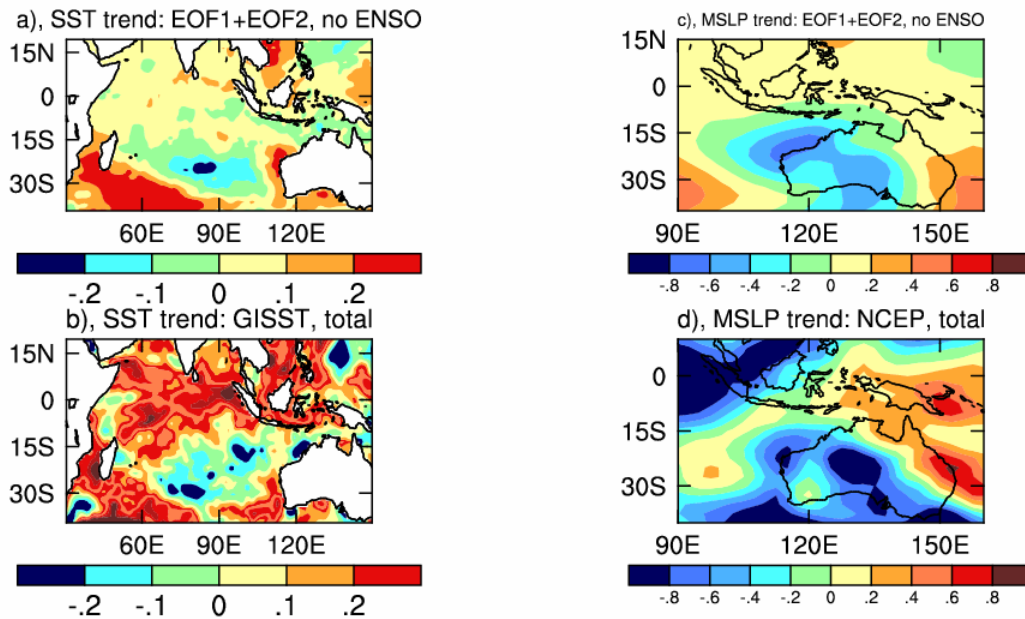


Figure 11: Panel a), SST trend ($^{\circ}\text{C}$) resulting from the sum of trends associated with DJF rainfall EOF1 and EOF2 of DJF rainfall shown in Fig.6. These trends are calculated by projecting raw DJF SST anomalies onto time series of the DJF rainfall EOFs (see text for details). Panel b), the total trend of raw SST. Panels c) and d), the same as a) and b) except for MSLP. A uniform value 0.35°C is taken out from b) and a value of 1.4 mb is subtracted from d), respectively.

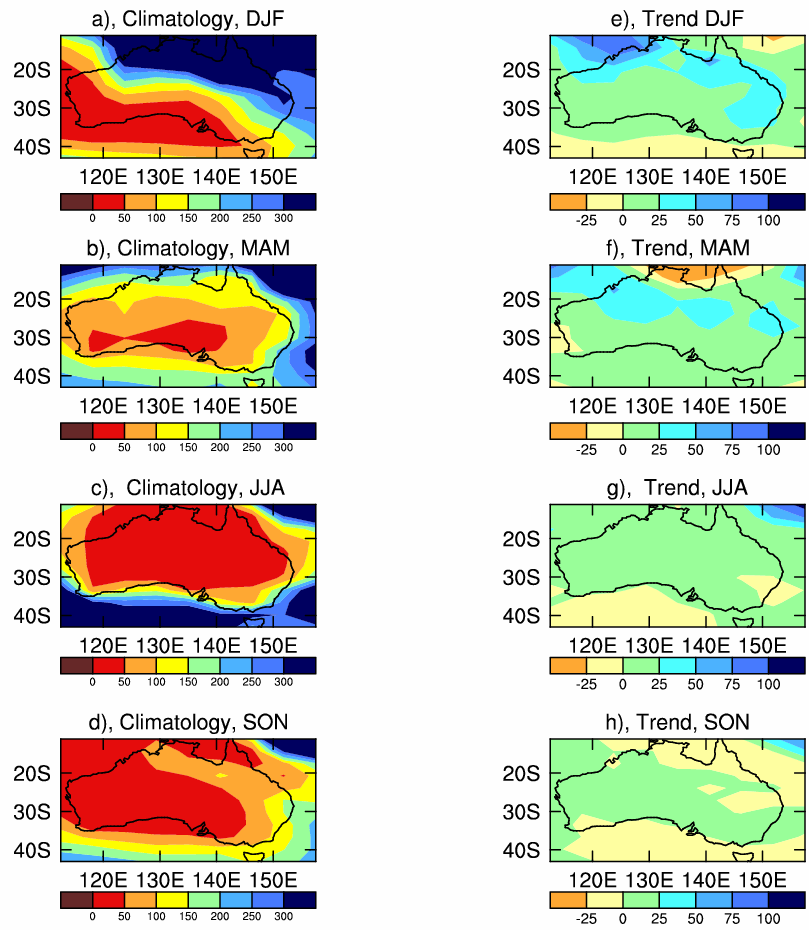


Figure 12: Model climatology (left column) from a 300-year control experiment of seasonal total rainfall (mm) and trend (right column) in seasonal total rainfall (mm) for 1951-2000.. The data are stratified into December-January-February (DJF), March-April-May (MAM), June-July-August (JJA), and September-October-November (SON).

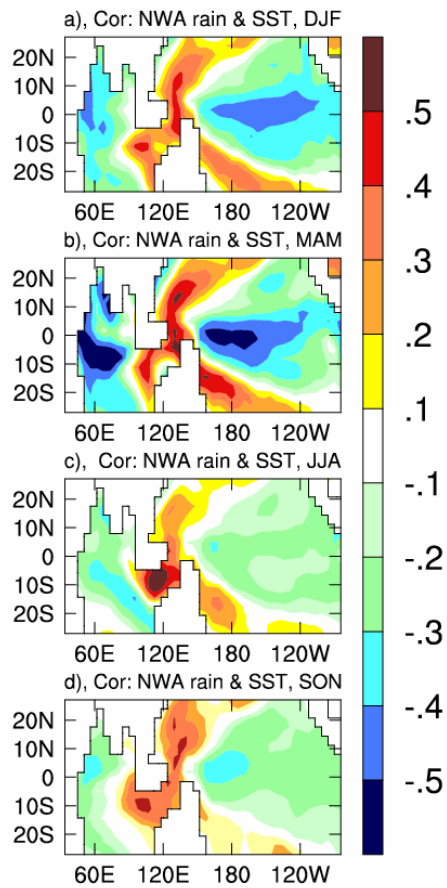


Figure 13: Map of correlation between modeled NWA rainfall and model grid-point SST (both linearly detrended) for each season using outputs from a 300-year control experiment. Correlation coefficients greater than 0.12 are significant at a 95% confidence level.

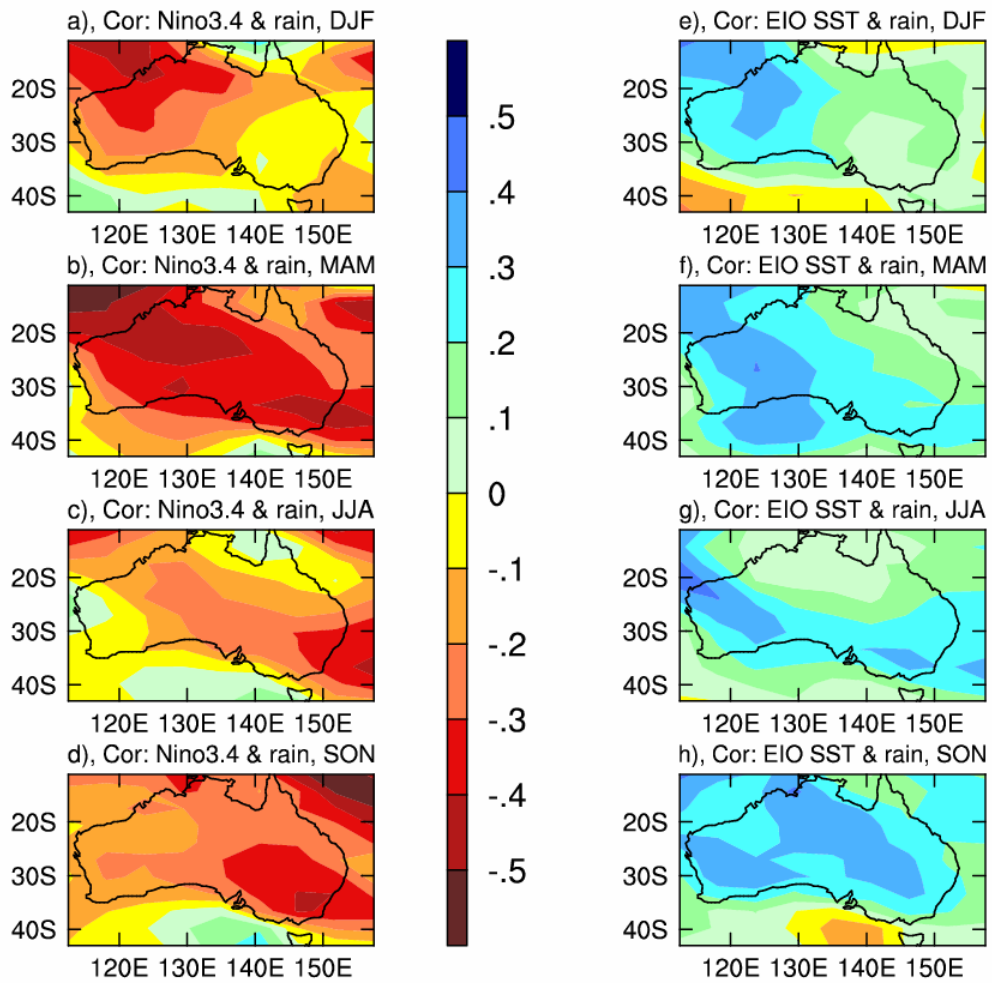


Figure 14: Maps of correlation of Australian rainfall with Nino3.4 (left column) and with EIO SST (right column) for each season using outputs from a 300-year control experiment model outputs.

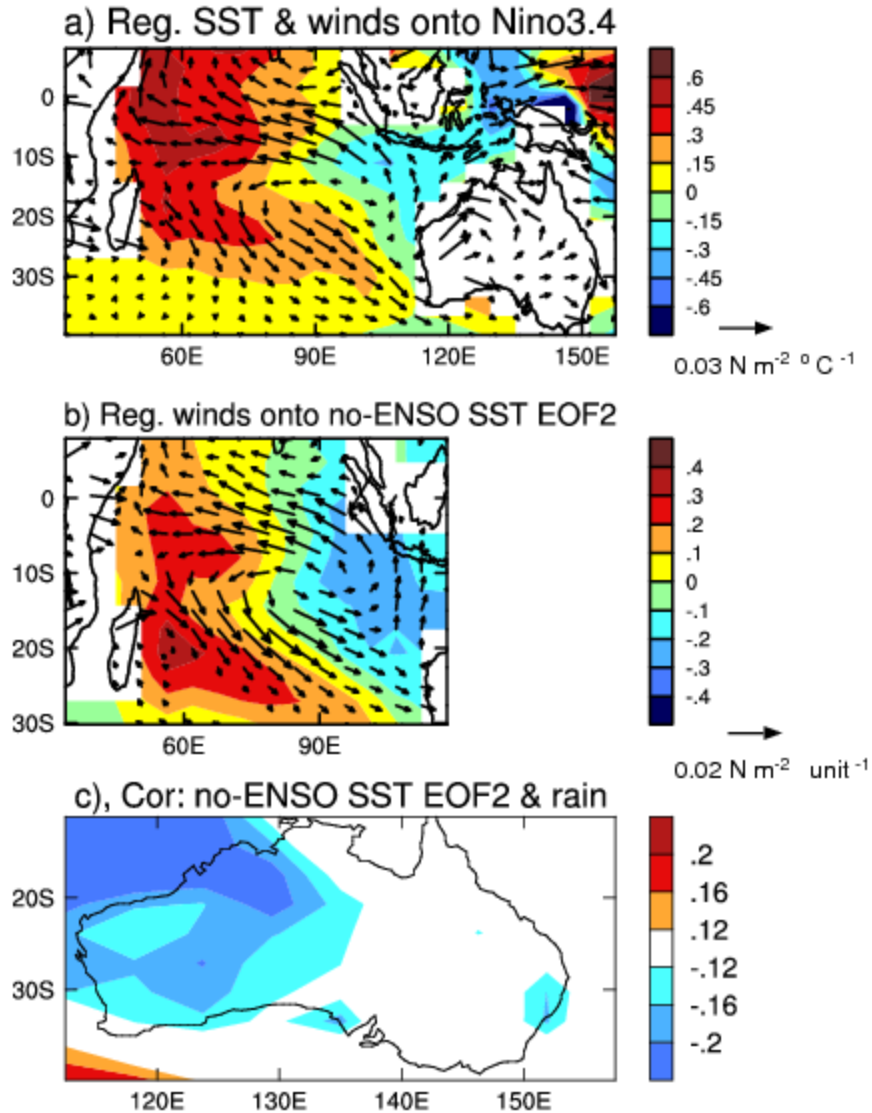


Figure 15: Panel a), pattern of model SST ($^{\circ}\text{C} \text{ }^{\circ}\text{C}^{-1}$, contour) and wind ($\text{N m}^{-2} \text{ }^{\circ}\text{C}^{-1}$, vectors) anomalies associated with model ENSO-like variability. These are obtained by regressing model SST and wind anomalies onto the model Nino3.4 index in the 300-year control experiment. Panel b), EOF2 (16.8% of the remaining variance) of model SST and the associated model wind fields (vectors) after removing variance associated with ENSO-like variability, and c), correlation between time series of model EOF2 shown in b) and model rainfall.

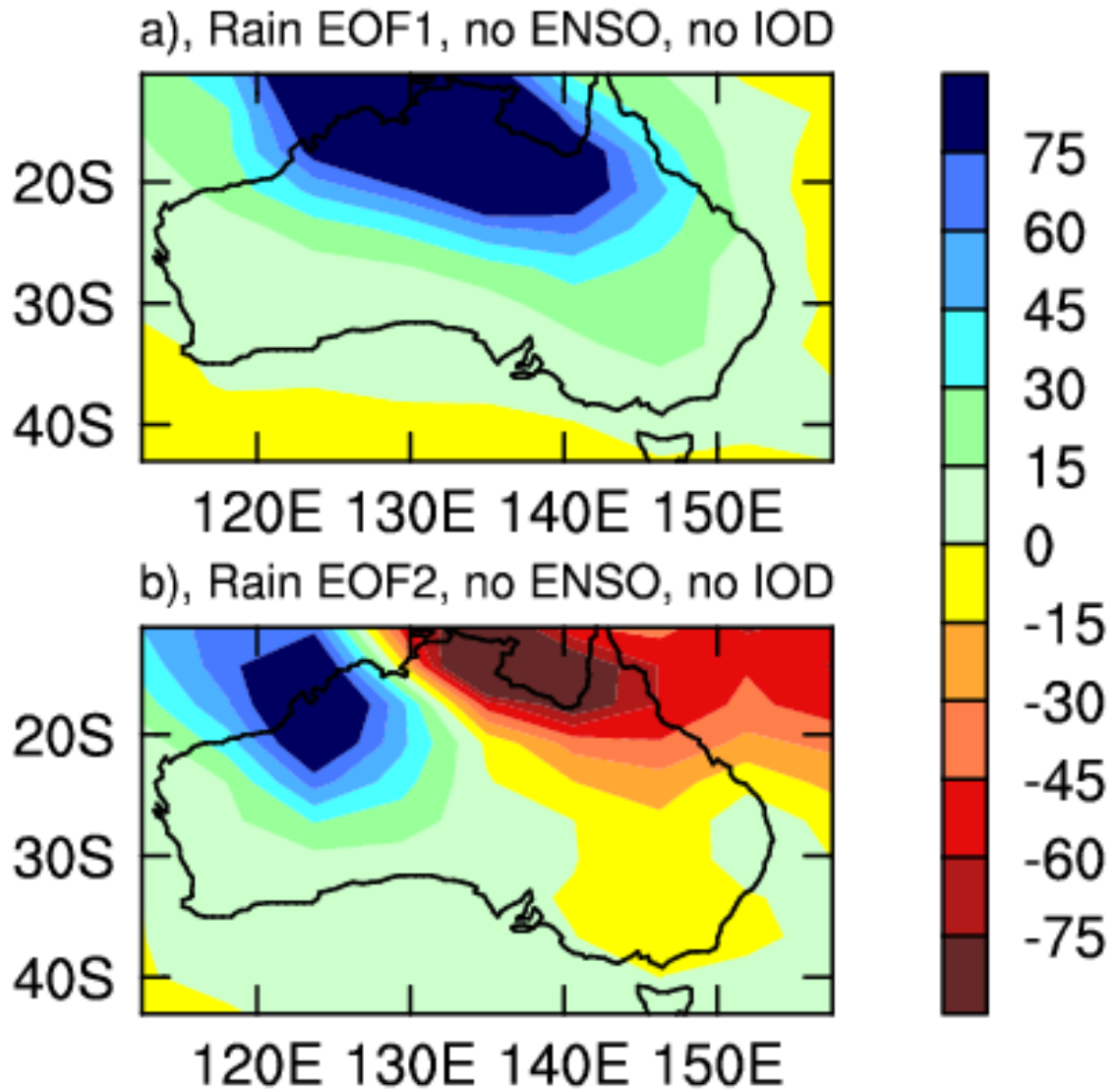


Figure 16: Patterns of model rainfall EOF after removing variances associated with ENSO and IOD (see text for details). Patterns are obtained by regressing rainfall anomalies onto the time series of the model EOF1 and EOF2 in the domain of 110°E-135°E, 10°S-25°S. EOFs 1 and 2 account for 47.6% and 20.7% of the remaining anomalies.

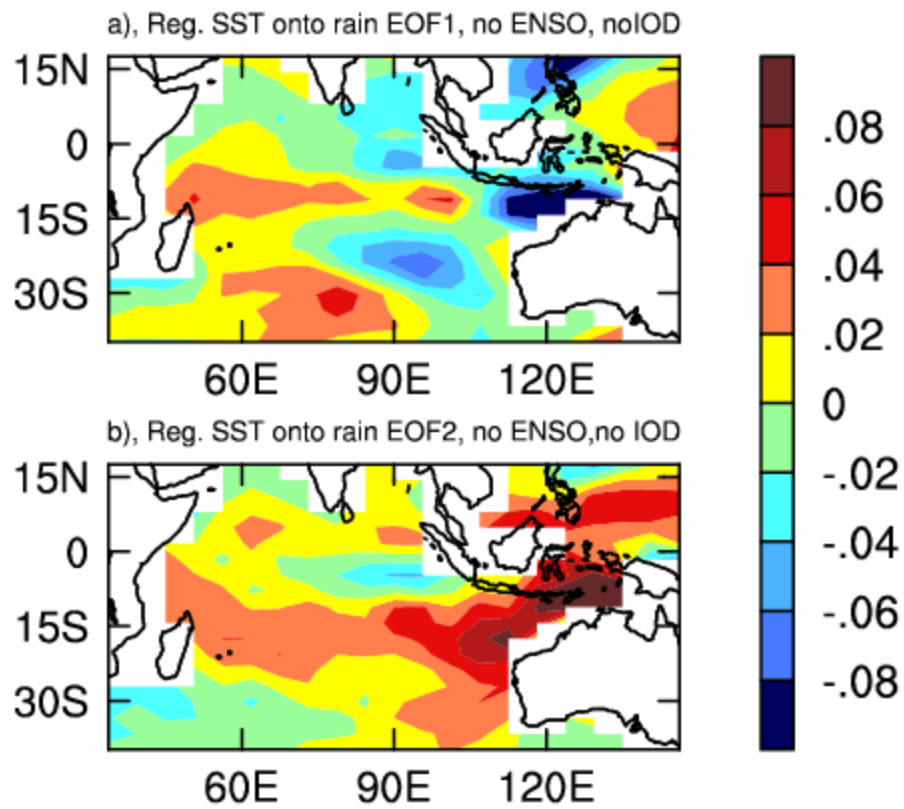


Figure 17: SST patterns associated with model rainfall EOF1 and EOF2 shown in Fig. 16. Patterns are obtained by regressing model SST anomalies onto the time series of the EOF1 and EOF2.

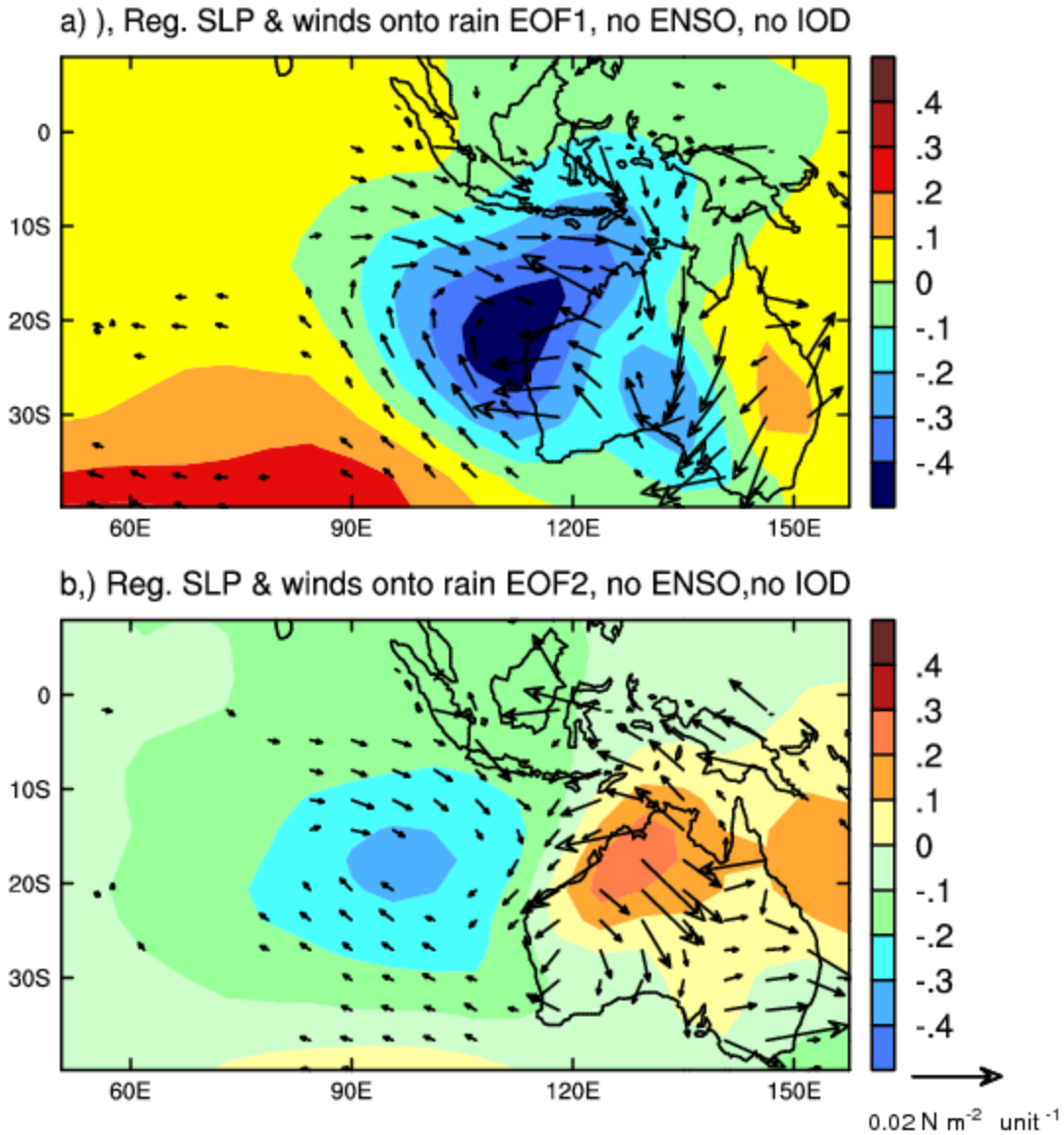


Figure 18: Anomaly patterns of MSLP (mb per unit of EOF time series) and winds (N m^{-2} per unit of EOF time series) associated with DJF rainfall EOF1 and EOF2 in the 300-year control experiment. Patterns are obtained by regressing model MSLP anomalies onto the time series of the rainfall EOFs.

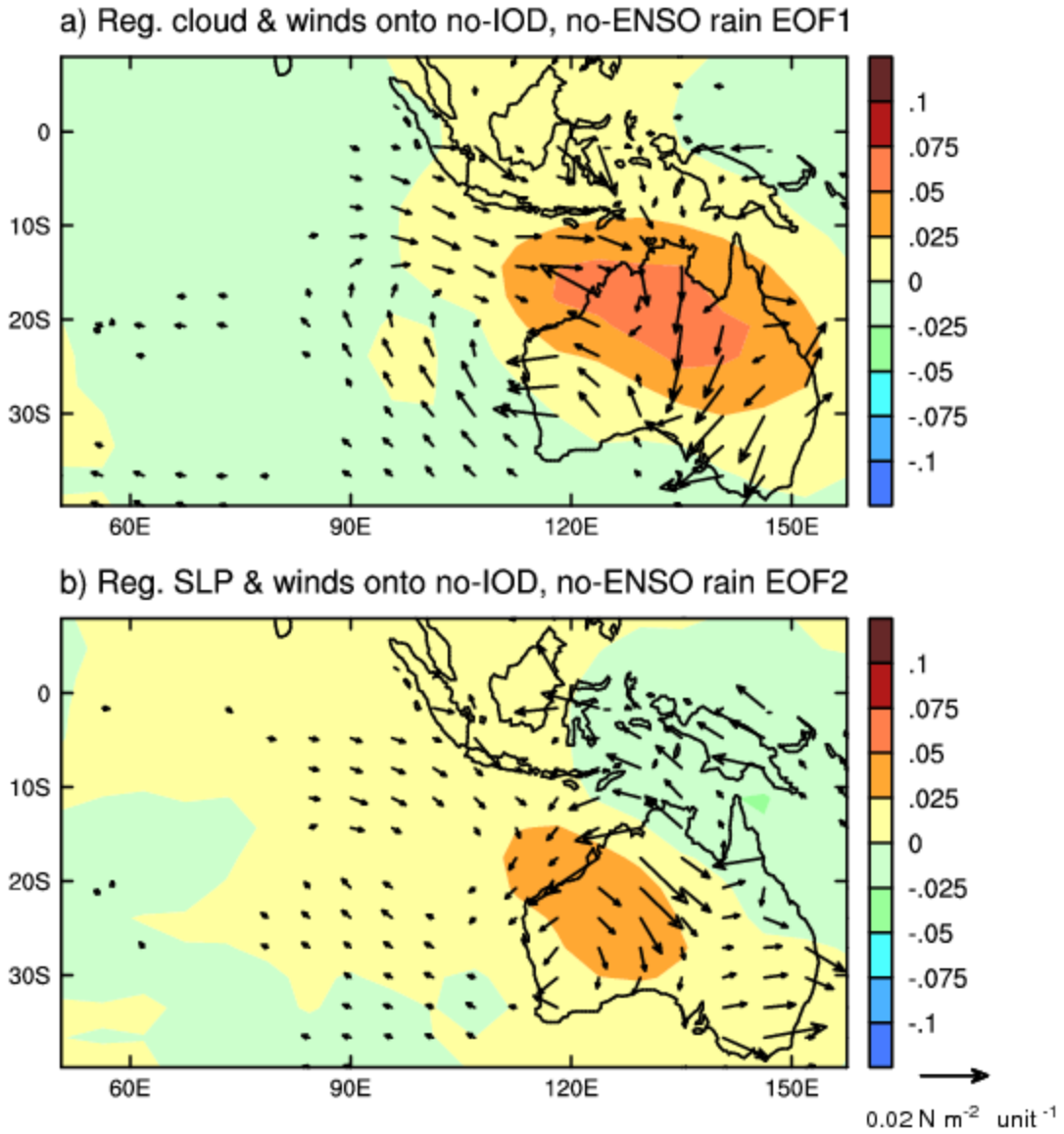


Figure 19: As in Figure 18, but for the cloud cover.

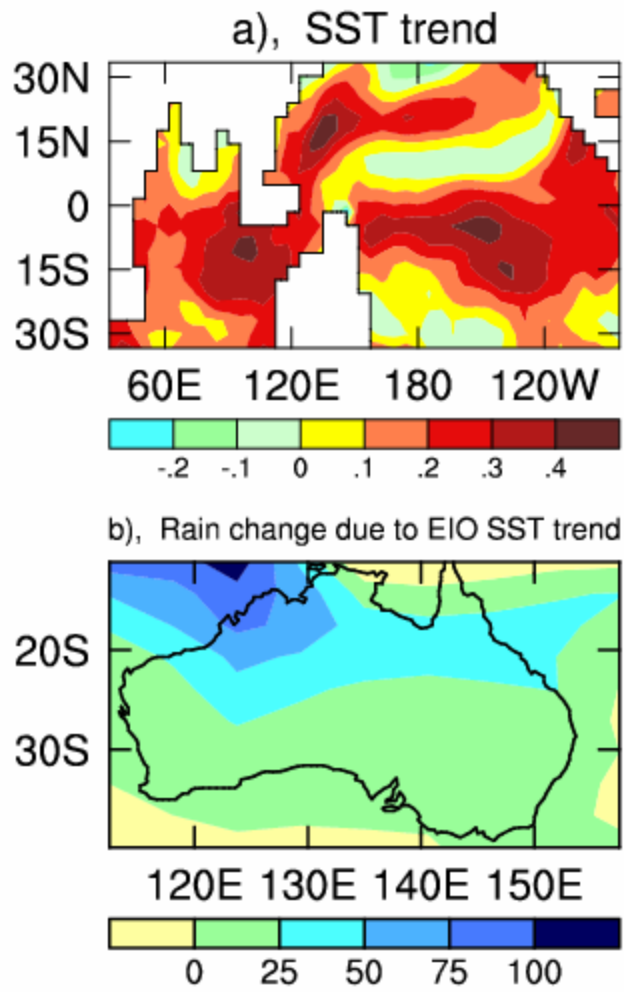


Figure 20: Panel a), Model DJF SST trend pattern ($^{\circ}\text{C}$) with all forcing imposed (ALL ensemble). Panel b), total trend (mm) of the DJF rainfall estimated from the unrealistic relationship between EIO SST and Australian rainfall in the 300-year control experiment.